Project Report
ATC-340

Detection Probability Modeling for Airport Wind-Shear Sensors

John Y. N. Cho
Robert G. Hallowell

August 28, 2008

Lincoln Laboratory

MASSACHUSETTS INSTITUTE OF TECHNOLOGY

Lexington, Massachusetts

Prepared for the Federal Aviation Administration,
Washington, DC 20591

This document is available to the public through
the National Technical Information Service,
Springfield, VA 22161

ABSTRACT

An objective wind-shear detection probability estimation model is developed for radar, lidar, and sensor combinations. The model includes effects of system sensitivity, site-specific wind-shear, clutter, and terrain blockage characteristics, range-aliased obscuration statistics, antenna beam filling and attenuation, and signal processing differences, which allow a sensor- and site-specific performance analysis of deployed and future systems. A total of 161 sites are analyzed for the study, consisting of airports currently serviced by the Terminal Doppler Weather Radar (TDWR) (46), Airport Surveillance Radar Weather Systems Processor (ASR-9 WSP) (35), Low Altitude Wind Shear Alert System-Relocation/Sustainment (LLWAS-RS) (40), and no wind-shear detection system (40). Sensors considered are the TDWR, WSP, LLWAS, Weather Surveillance Radar 1988-Doppler (WSR-88D, commonly known as NEXRAD), and the Lockheed Martin Coherent Technologies (LMCT) Doppler lidar and proposed X-band radar.

The results show that the TDWR is the best single-sensor performer for microburst and gust-front detection among the considered wind-shear sensing systems. Also, preexisting TDWRs are close enough to four non-TDWR airports to provide satisfactory wind-shear detection capability (MCO for ORL and SFB, ATL for PDK, and TPA for PIE). On its own, the ASR-9 WSP cannot provide the required 90% microburst detection probability at many airports, even after the planned upgrade to its clutter suppression capability. The NEXRAD is too far away at a majority of airports to provide adequate wind-shear detection coverage. The typical LLWAS detection probability for microbursts was low (~50%), because the anemometers usually only covered a fraction of the Areas Noted for Attention (ARENAs). In fact, the only LLWAS airport with full microburst coverage was Denver (97% detection probability).

Although the lidar by itself does not yield impressive wind-shear detection statistics, in combination with a radar it is projected to form an optimal configuration for wind-shear detection over the ARENAs and beyond. This is because the lidar excels at wind-shear detection under low reflectivity conditions when the radar signal is weak, and its collimated beam avoids ground clutter on which the radar's diverging antenna beam impinges. An LLWAS added to a radar can also improve the microburst detection probability over the ARENAs, but not to the same extent as a lidar if the radar detection probability is not very high. The LLWAS also cannot contribute to wide-area surveillance (beyond the ARENAs) because it is a collection of localized in situ instruments.

TABLE OF CONTENTS

LIST OF ILLUSTRATIONS

LIST OF ILLUSTRATIONS (Continued)

LIST OF TABLES

LIST OF TABLES (Continued)

1. INTRODUCTION

Low-level wind shear, especially a microburst, is very hazardous to aircraft departing or approaching an airport. The danger became especially clear in a series of fatal commercial airliner accidents in the 1970s and 1980s at U.S. airports. In response, the Federal Aviation Agency (FAA) developed and deployed three ground-based low-altitude wind-shear detection systems: the Low Altitude Wind Shear Alert System (LLWAS) (Wilson and Gramzow 1991), the Terminal Doppler Weather Radar (TDWR) (Michelson et al. 1990), and the Airport Surveillance Radar Weather Systems Processor (ASR-9 WSP) (Weber and Stone 1995). Since the deployment of these sensors, commercial aircraft wind-shear accidents have dropped to near zero in the U.S. This dramatic decrease in accidents caused by wind shear appears to confirm the safety benefits provided by these detection systems. In addition, the broad area measurement capability of the TDWR and WSP provides delay reduction benefits, e.g., by forecasting airport wind shifts that may require runway reconfiguration.

The current deployment strategy for these various wind-shear detection systems is justified by an earlier integrated wind-shear systems cost-benefit analysis (Martin Marietta 1994). Since that time, conditions in the national airspace system (NAS) have evolved, such as the installation of onboard predictive wind-shear detection systems in an increasing number of aircraft, improved pilot training for wind-shear hazard identification, avoidance, and recovery, and further integration of observed wind-shear data into terminal weather systems. Given the tight fiscal environment at the FAA in recent years, the cost of maintaining the wind-shear detection systems has also become an issue. All systems require periodic service life extension programs (SLEPs) in order to keep them operating. If new systems are to be developed instead of performing SLEPs on the existing ones, many years of lead time is necessary to assure a smooth transition. In light of these considerations, the FAA has tasked MIT Lincoln Laboratory to provide an updated cost-benefit study on their terminal wind-shear detection systems.

One of the key factors in estimating the benefits of a terminal wind-shear detection system is its performance. Thus, it is necessary to quantify the wind-shear detection probability for each sensor, preferably on an airport-by-airport basis. To consider sensors that are not yet deployed models must be developed that take into account the various effects that factor into the detection probability. This report provides the details of such models and the results obtained with them.

2. SCOPE OF STUDY

In addition to the three FAA wind-shear detection systems mentioned above, we included the Weather Surveillance Radar 1988-Doppler (WSR-88D, commonly known as NEXRAD) (Heiss et al. 1990) in this study. Although not specifically deployed to be a terminal wind-shear detection radar, the NEXRAD is a high-performance weather radar that is capable of providing useful wind-shear data if it is located close enough to an airport.

Furthermore, we considered new sensors in addition to the currently deployed systems. The Lockheed Martin Coherent Technologies (LMCT) Wind Tracer lidar is a commercially available product that has been operationally deployed at the Hong Kong International Airport along with a TDWR (Chan et al., 2006). For reasons to be explained later, it has been suggested as a complementary sensor at major U.S. airports where radar alone has not been yielding satisfactory wind-shear detection performance. (The FAA has recently decided to purchase one for the Las Vegas airport.) To offer a stand-alone wind-shear detection package, LMCT has proposed an X-band radar to go along with the lidar, so we included this sensor in our analysis.

Looking into the future, another alternative to maintaining or replacing these wind-shear sensors is the wholesale replacement of all civil-sector weather and aircraft surveillance radars with a multi-mission phased array radar (MPAR) network (Weber et al. 2007). Ideally we would have included the MPAR in this study, but, at this time, the MPAR requirements and parameters are in flux, so we felt that it would be premature to run a detailed comparative analysis on such a system.

The wind-shear phenomena for which we computed detection probabilities are the microburst and gust front. There are, in fact, other forms of hazardous wind-shear, such as gravity waves, but these are the only ones for which FAA detection requirements exist at this time. The detection coverage areas assumed was the union of the Areas Noted for Attention (ARENAs) for microbursts and an 18-km-radius circle around the airport for gust fronts (Figure 2-1). An ARENA polygon consists of the runway length plus three nautical miles final on approach and two nautical miles on departure times a width of one nautical mile. The 18-km extent of the gust-front coverage corresponds to the distance a gust front would travel at 15 m s^{-1} for 20 minutes, which is an appropriate metric for gust-front anticipation lead time in the context of airport operations. Gust-front detection is important for delay reduction benefits. (For reference, the TDWR generates gust-front products out to 60 km from the airport.)

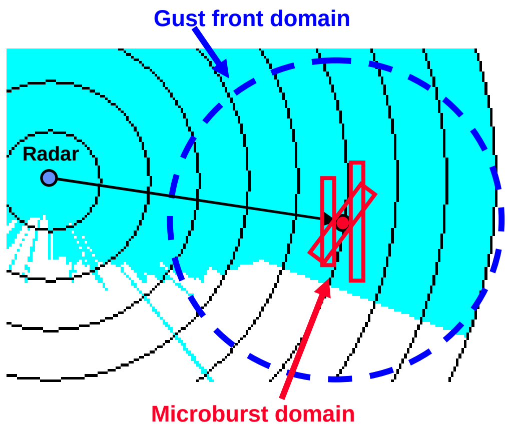

Figure 2-1. Wind-shear coverage domains used in study. White space illustrates terrain blockage.

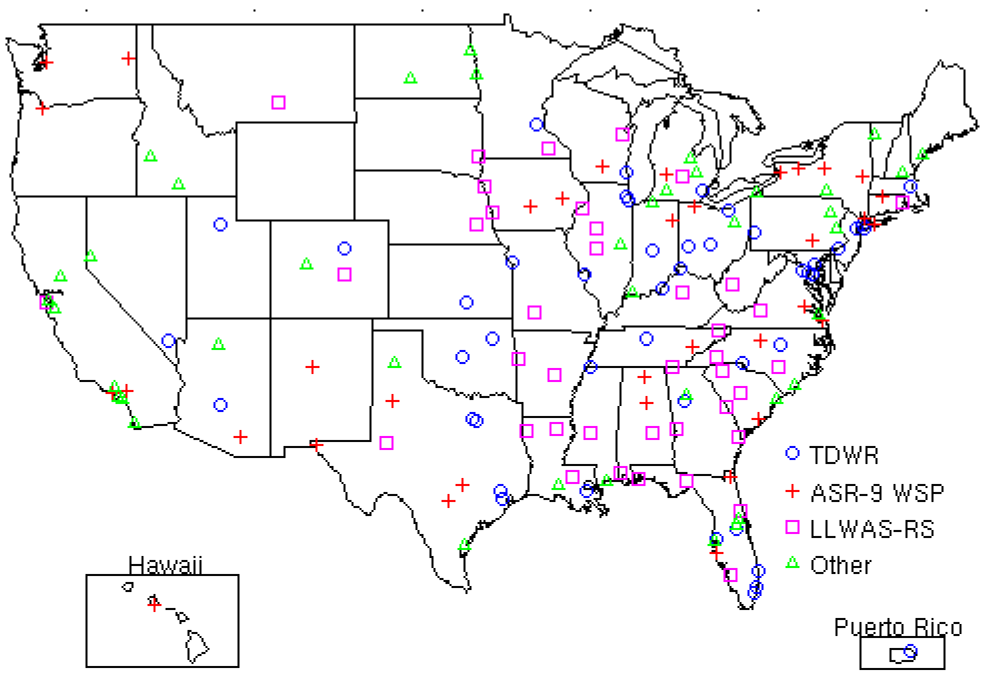

Figure 2-2. Locations of the 161 airports included in this study.

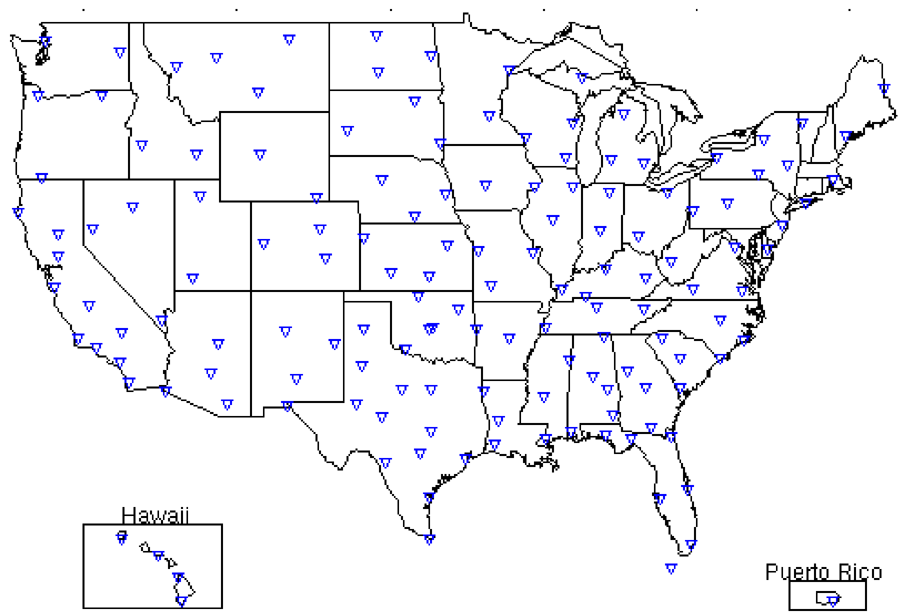

Figure 2-3. NEXRAD locations.

Airports that presently have coverage by TDWR (46), ASR-9 WSP (35), and LLWAS-RS (Relocation/Sustainment) (40) were selected for this study. An additional 40 airports without wind-shear sensors were included, based on a change in FAA policy to also protect non-Part-121 aircraft from wind shear hazards. Heretofore in this report, these 40 airports will be called the “other” airports. The locations of these 161 airports are shown in Figure 2-2, while the locations of the NEXRADs are displayed in Figure 2-3. Table 2-1 shows which sensors already exist at which airports, and which sensors are considered for new deployment at which airports. We did not consider the possibility of installing new TDWRs or ASR-9s due to prohibitive cost; new WSPs are only considered for already existing ASR-9s. Deploying new or moving existing NEXRADs was not considered. Although the TDWR and the WSP are nominally considered for the other airports, there are, in fact, only a few sites that have a TDWR or ASR-9 close enough to be useful for wind-shear detection.

TABLE 2-1

Sensors vs. Airports Included in Study

Sensor	Airport (161)			
	TDWR (46)	WSP (35)	LLWAS-RS (40)	Other (40)
TDWR	Existing	N/A	N/A	Existing*
WSP	New	Existing	N/A	Existing*
LLWAS	Existing (9) New (37)	New	Existing	New
NEXRAD	Existing*	Existing*	Existing*	Existing*
LMCT Lidar	New	New	New	New
LMCT X band	New	New	New	New

*Closest to airport.

Wind-shear detection performances of sensor combinations were also analyzed (see Table 2-2). Again, cost-prohibitive alternatives were not considered.

TABLE 2-2

Sensor Combination vs. Site

Sensor Combination	Site
TDWR + lidar	TDWR and other airports
TDWR + LLWAS	TDWR and other airports
TDWR + NEXRAD	TDWR and other airports
WSP + lidar	TDWR, WSP, and other airports
WSP + LLWAS	TDWR, WSP, and other airports
WSP + NEXRAD	TDWR, WSP, and other airports
WSP + NEXRAD + lidar	TDWR, WSP, and other airports
WSP + NEXRAD + LLWAS	TDWR, WSP, and other airports
NEXRAD + lidar	All airports
NEXRAD + LLWAS	All airports
X-band + lidar	All airports
X-band + LLWAS	All airports

Note that, at the present time, NEXRADs are not suitable for microburst detection and warning, because their update rates (~5 minutes) are too slow to meet the FAA requirement. (For gust-front detection and tracking, the update rates are adequate, and the FAA already takes advantage of NEXRAD data for this purpose (Smalley et al. 2005).) Thus, even though the NEXRAD microburst detection probabilities we estimate in this study may, in some cases, appear to be acceptable, actual operational use would require that a substantially faster volume scan strategy be implemented. As a triagency radar with the FAA as a minor stakeholder, it may be problematic to prioritize the NEXRAD for terminal microburst detection in this way. In the future, an MPAR could make such multitasking a reality.

Table 2-3 lists the study airports, the IDs of the closest radars, and the distances between them.

TABLE 2-3

Closest Radar Distance to Airport

Airport	TDWR	ASR-9	NEXRAD	Distance to Airport (km)			Airport	TDWR	ASR-9	NEXRAD	Distance to Airport (km)		
				TDWR	ASR-9	NEXRAD					TDWR	ASR-9	NEXRAD
ABE	PHL	PHL	DIX	84.2	89.3	117.4	LAX	LAS	LAX	SOX	394.8	1.1	72.8
ABQ	PHX	ABQ	ABX	542.2	1.1	23.0	LBB	OKC	LBB	LBB	434.7	2.9	1.4
ADW	ADW	ADW	LWX	13.0	0.2	56.1	LEX	SDF	SDF	LVX	88.2	100.0	117.7
AGS	ATL	CHS	CAE	215.7	187.7	101.4	LFT	MSY	MSY	LCH	154.0	168.7	118.6
ALB	JFK	ALB	ENX	239.9	1.7	28.1	LGA	JFK	JFK	OKX	20.9	17.7	85.6
AMA	OKC	LBB	AMA	381.9	172.6	1.6	LGB	LAS	LGB	SOX	386.0	14.1	47.7
ASE	DEN	GJT	GJX	209.2	139.2	117.6	LIT	MEM	MEM	LZK	205.0	210.9	12.4
ATL	ATL	ATL	FFC	15.3	1.3	33.3	LNK	MCI	OFF	OAX	228.2	79.0	61.7
AUS	IAH	AUS	EWX	203.1	1.8	64.5	MAF	DAL	SJT	MAF	504.1	175.3	1.2
AVL	CLT	TYS	GSP	150.9	139.4	68.0	MBS	DTW	PTK	DTX	164.5	126.2	104.9
AVP	EWR	SWF	BGM	147.7	136.3	98.1	MCI	MCI	MCI	EAX	22.4	2.0	66.7
AZO	DTW	GRR	GRR	168.9	71.1	73.2	MCO	MCO	MCO	MLB	9.6	3.9	73.2
BDL	BOS	BDL	OKX	146.9	0.1	120.2	MDT	BWI	MDT	CCX	123.1	2.9	132.7
BGM	EWR	SYR	BGM	229.4	100.9	1.1	MDW	MDW	QXM	LOT	15.1	18.3	34.2
BHM	ATL	BHM	BMX	231.4	1.2	43.4	MEM	MEM	MEM	NQA	16.3	3.3	34.8
BIL	SLC	MSO	BLX	603.6	445.1	7.1	MGM	ATL	MXF	MXX	249.0	10.3	62.6
BIS	MSP	MSP	BIS	642.5	620.0	1.1	MHT	BOS	AL6	BOX	95.4	11.3	111.2
BNA	BNA	BNA	OHX	16.1	0.3	17.1	MIA	MIA	MIA	AMX	20.5	0.5	23.7
BOI	SLC	MSG	CBX	456.7	309.7	8.3	MKE	MKE	MKE	MKX	18.7	1.9	53.4
BOS	BOS	BOS	BOX	23.6	1.7	46.7	MLI	ORD	CID	DVN	224.1	110.8	19.1
BTR	MSY	MSY	LIX	91.5	104.7	129.1	MLU	MSY	BAD	SHV	316.9	152.3	170.0
BTV	BOS	ALB	CXX	313.8	199.6	4.5	MOB	MSY	MSY	MOB	220.6	208.0	1.3
BUF	PIT	BUF	BUF	307.7	0.3	1.0	MSN	MKE	MSN	MKX	111.2	1.5	66.9
BUR	LAS	BUR	VTX	373.7	0.5	79.0	MSP	MSP	MSP	MPX	22.5	1.3	27.8
BWI	BWI	BWI	LWX	10.1	1.4	73.5	MSY	MSY	MSY	LIX	14.4	0.6	56.4
CAE	CLT	CLT	CAE	156.7	142.4	1.1	MYR	CLT	CHS	LTX	257.1	136.9	57.6
CAK	CLE	CLE	CLE	63.1	64.2	65.4	OAK	LAS	OAK	MUX	665.9	1.7	69.0
CHA	BNA	TYS	HTX	168.7	138.5	81.2	OKC	OKC	OKC	CRI	15.4	2.3	21.5
CHS	CLT	CHS	CLX	281.5	2.7	97.6	OMA	MCI	OFF	OAX	223.0	17.8	40.0
CID	MKE	CID	DVN	319.2	0.5	98.8	ONT	LAS	ONT	SOX	331.0	0.8	26.6
CLE	CLE	CLE	CLE	18.9	0.9	0.9	ORD	ORD	ORD	LOT	20.5	2.0	44.2
CLT	CLT	CLT	GSP	14.7	0.4	122.1	ORF	ADW	ORF	AKQ	207.8	0.7	72.5
CMH	CMH	CMH	ILN	15.1	1.1	102.3	ORL	MCO	MCO	MLB	22.4	16.9	82.0
CMI	IND	IND	ILX	163.9	174.2	91.1	PBI	PBI	FLL	AMX	17.7	68.4	123.0
COS	DEN	DAB	PUX	103.4	116.5	59.4	PDK	ATL	ATL	FFC	25.7	29.8	61.9
CRP	HOU	HRL	CRP	293.7	179.3	1.8	PDX	SLC	PDX	RTX	1005.4	2.2	31.8
CRW	CMH	CMH	RLX	205.5	213.5	13.3	PHF	ADW	ORF	AKQ	176.3	37.4	48.6
CSG	ATL	ATL	MXX	140.4	132.2	80.0	PHL	PHL	PHL	DIX	17.0	2.6	71.5
CVG	CVG	CVG	ILN	18.0	0.8	83.7	PHX	PHX	PHX	IWA	14.1	1.4	35.6
DAB	MCO	MCO	MLB	96.3	90.3	124.7	PIA	MDW	QXM	ILX	198.0	193.3	64.6
DAL	DAL	QZB	FWX	14.0	15.6	52.1	PIE	TPA	TPA	TBW	17.6	16.5	36.1
DAY	DAY	DAY	ILN	15.6	2.0	63.5	PIT	PIT	PIT	PBZ	21.5	3.3	4.6

DCA	DCA	DCA	LWX	12.3	0.9	83.7	PNS	MSY	QZR	MOB	313.6	167.0	103.6
DEN	DEN	DVX	FTG	19.5	3.9	13.8	PVD	BOS	PVD	BOX	63.3	14.1	35.3
DFW	DFW	DFW	FWS	21.7	2.9	43.7	PWM	BOS	CUM	GYX	173.0	20.3	27.6
DSM	MCI	DSM	DMX	243.8	1.1	22.5	RDU	RDU	RDU	RAX	16.0	1.0	35.8
DTW	DTW	DTW	DTX	17.5	2.2	55.0	RIC	ADW	RIC	AKQ	138.5	0.4	64.1
ELP	PHX	ELP	EPZ	571.6	1.8	31.2	RNO	LAS	BAB	RGX	560.6	151.6	38.7
ERI	CLE	BUF	BUF	176.0	152.0	152.5	ROA	RDU	LYH	FCX	186.1	71.0	42.7
EVV	SDF	HOP	LVX	168.7	151.4	139.7	ROC	PIT	ROC	BUF	373.0	0.6	88.8
EWR	EWR	EWR	DIX	14.0	2.5	85.3	RST	MSP	MSP	ARX	112.4	123.6	105.6
FAR	MSP	MSP	MVX	377.7	358.2	77.8	RSW	FLL	SRQ	TBW	147.4	123.6	144.5
FAY	RDU	FAY	RAX	113.4	33.0	82.8	SAN	LAS	NKX	NKX	428.1	17.2	24.8
FLL	FLL	FLL	AMX	20.7	0.5	57.5	SAT	IAH	SAT	EWX	286.7	2.8	46.7
FNT	DTW	PTK	DTX	96.7	57.8	36.9	SAV	ATL	CHS	CLX	332.2	137.0	60.4
FSD	MSP	OFF	FSD	336.3	280.0	1.2	SBN	MDW	QXM	IWX	117.8	121.3	64.5
FSM	TUL	FYV	SRX	155.1	74.0	5.1	SDF	SDF	SDF	LVX	18.0	1.6	28.7
FWA	DAY	FWA	IWX	139.8	1.4	59.8	SEA	SLC	SEA	ATX	1096.9	0.6	84.1
GCN	LAS	LSV	FSX	258.6	261.9	175.6	SFB	MCO	MCO	MLB	48.9	42.9	93.2
GEG	SLC	GEG	OTX	863.4	1.4	9.7	SFO	LAS	OAK	MUX	676.7	16.4	66.6
GFK	MSP	MSP	MVX	472.6	255.6	48.1	SGF	TUL	FYV	SGF	254.0	156.0	1.5
GPT	MSY	MSY	LIX	135.3	122.7	73.0	SHV	DFW	BAD	SHF	297.8	17.3	1.5
GRB	MKE	MKE	GRB	185.1	172.2	2.1	SJC	LAS	NUQ	MUX	632.6	10.3	23.2
GRR	DTW	GRR	GRR	185.9	0.7	2.3	SJU	SJU	MIA	JUA	19.2	1682.8	36.7
GSO	RDU	GSO	FCX	112.2	2.3	107.1	SLC	SLC	SLC	MTX	20.3	2.6	65.9
GSP	CLT	CLT	GSP	131.1	121.3	1.4	SMF	LAS	MCC	DAX	647.7	16.5	22.8
HNL	LAS	HNL	HMO	4459.8	0.6	79.7	SNA	LAS	LGB	SOX	378.5	17.9	26.7
HOU	HOU	HOU	HGX	14.8	3.1	27.3	SPI	STL	STL	ILX	134.9	136.3	44.8
HPN	JFK	HPN	OKX	55.1	0.9	74.4	SRQ	TPA	SRQ	TBW	51.6	0.4	37.5
HSV	BNA	HSV	HTX	149.3	1.2	71.2	STL	STL	STL	LSX	12.9	1.2	28.6
IAD	IAD	IAD	LWX	16.7	1.5	3.9	SUX	MCI	OFF	OAX	350.9	145.5	120.2
IAH	IAH	IAH	HGX	23.5	1.9	62.2	SYR	EWR	SYR	TYX	318.5	0.1	79.5
ICT	ICT	ICT	ICT	15.9	0.8	1.0	TLH	TPA	QZR	TLH	333.0	162.6	2.1
ILM	RDU	FAY	LTX	205.3	149.1	57.8	TOL	DTW	TOL	DTX	63.1	0.4	126.7
IND	IND	IND	IND	15.1	1.7	1.6	TPA	TPA	TPA	TBW	12.9	1.8	32.6
ISP	JFK	ISP	OKX	69.8	1.3	21.4	TRI	CLT	TYS	MRX	186.6	161.9	95.6
JAN	MSY	MSY	DGX	255.8	257.1	9.3	TUL	TUL	TUL	INX	15.2	3.1	29.2
JAX	MCO	JAX	JAX	240.9	0.5	1.7	TUS	PHX	TUS	EMX	184.5	7.1	38.3
JFK	JFK	JFK	OKX	10.3	1.1	81.2	TWF	SLC	MSG	SFX	271.3	127.8	162.9
LAN	DTW	GRR	GRR	115.2	77.6	79.4	TYS	ATL	TYS	MRX	241.4	1.4	66.5
LAS	LAS	LAS	ESX	14.8	2.1	48.2							

3. RADAR PERFORMANCE ANALYSIS

Of the radar systems considered in this study (Figure 3-1), the TDWR has the best performance characteristics for terminal wind-shear detection—it has the highest weather sensitivity, the narrowest antenna beam (for clutter avoidance), and its use is 100% dedicated to this mission. It also incurs the highest cost to the FAA, because it is not shared with other agencies or missions, and it is located on its own site away from the airport. The WSP is a signal processing system that is piggybacked onto the ASR-9 terminal aircraft surveillance radar, so the incremental cost is quite low. However, being dependent on the vertical fan beam and rapid scanning rate of the ASR-9, it is far from an ideal system for low-level wind-shear detection. The NEXRAD is only slightly less sensitive to weather compared to the TDWR, has a 1° antenna beam, and its cost is shared by two other agencies besides the FAA. However, it is often not located close enough to the airport, and its volume scanning strategy, which is tailored to wide-area coverage, is too slow for microburst alerting. The proposed LMCT X-band radar should have performance and cost profiles that are somewhere in between the TDWR/NEXRAD and WSP extremes.

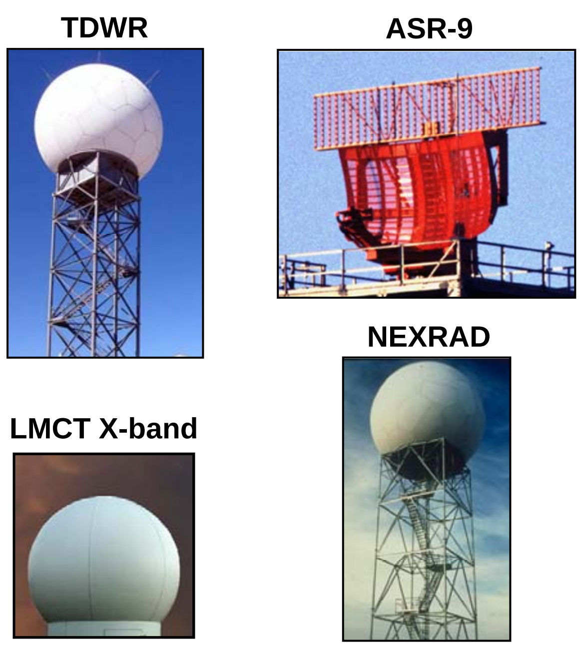

Figure 3-1. The radars included in this study.

The radar system sensitivity was the starting point of our analysis. Shown in Table 3-1 are some of the relevant system parameters and the minimum detectable dBZ at 50-km range for the four radars studied. Although the latter quantity does not include precipitation attenuation effects, in the analysis they were included at X band, where this effect can be significant.

Radar signal detection can be noise limited or clutter limited. In the latter case, the clutter suppression capability determines the detection performance. All three existing radars (TDWR, NEXRAD, ASR-9) which have klystron transmitters, are undergoing or expected to undergo an upgrade that will bring the maximum possible clutter suppression to about 60 dB. The LMCT X-band radar has a magnetron transmitter with an expected maximum clutter suppression capability of 50 dB (J. Roby, private communication). For the results used in the cost-benefit analysis we used the post-upgrade performance figures.

TABLE 3-1

Radar System Parameters

Parameter	TDWR	ASR-9 WSP	NEXRAD	LMCT X-band
Peak Power (kW)	250	1,120	750	200
Pulse Length (μs)	1.1	1	1.6	0.4
Antenna Gain (dB)	50	34	45.5	43
Beamwidth (Azimuth x Elevation)	0.55° x 0.55°	1.4° x 4.8°	0.925° x 0.925°	1.4° x 1.4°
Beam Elevation Angle	0.3°	2°	0.5°	0.7°
Wavelength (cm)	5.4	11	10.5	3.3
Max. Clutter Suppression (dB)	57 (60*)	48 (60*)	50 (60*)	50
Rotation Rate (°/s)	~ 20	75	~ 20	~ 20
Pulse Repetition Frequency (Hz)	~ 1600	~ 1100	~ 1000	~ 2500
Min. Detectable dBZ @ 50 km**	-11	7	-10	-3

*After upgrade.
**Without precipitation attenuation.

The ability of a radar system to detect low-altitude wind shear depends not only on the radar sensitivity and clutter suppression capability, but also on viewing geometry, clutter environment, signal processing and detection algorithm effectiveness, and the characteristics of the wind shear itself (Figure 3-2). Thus, although the system characteristics may be invariant with respect to location, there are many site-specific factors that affect the probability of detection (P_d) performance. In this study we tried to objectively account for as many of these factors as possible.

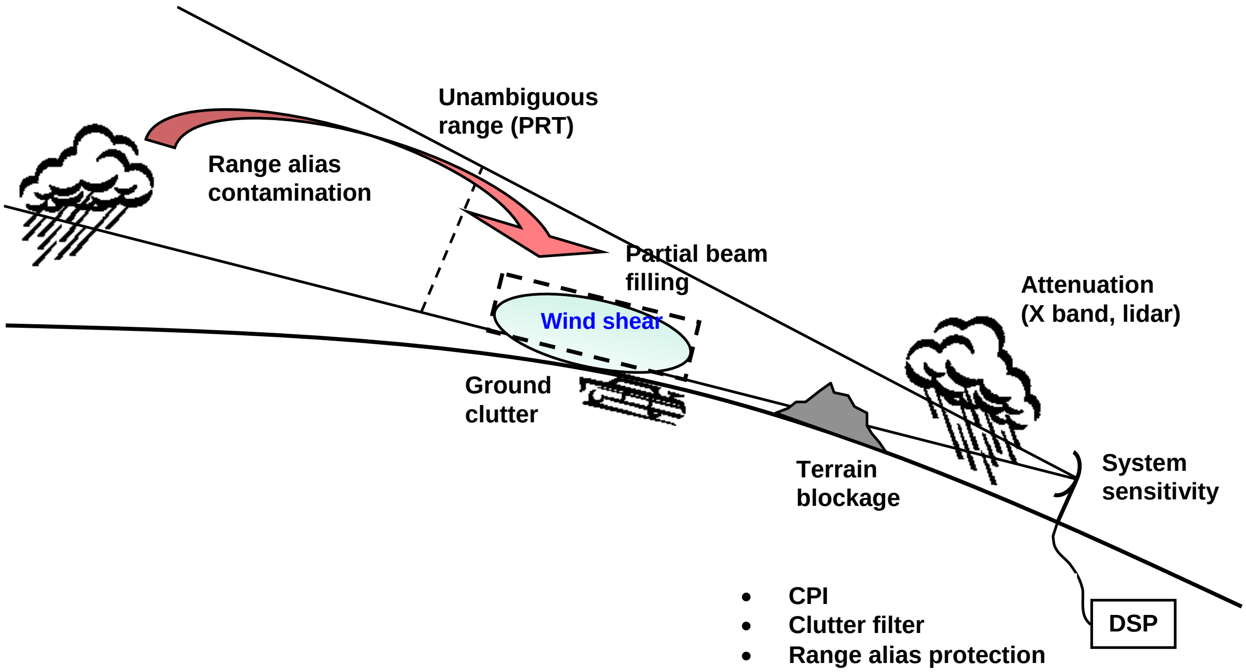

Figure 3-2. Illustration of various factors that impact radar wind-shear detection probability.

A high-level flow chart of the radar wind-shear P_d performance estimator is shown in Figure 3-3. For each radar at a given site, a clutter residue map (CREM) was generated using digital terrain elevation data (DTED), digital feature analysis data (DFAD), and radar characteristics (Appendix A). We chose this synthetic approach over using real CREMs, because CREMs were very difficult to access in some cases (e.g., ASR-9 WSP) and the scope of this study included hypothetical installations of new systems for which, obviously, there are no existing CREMs.

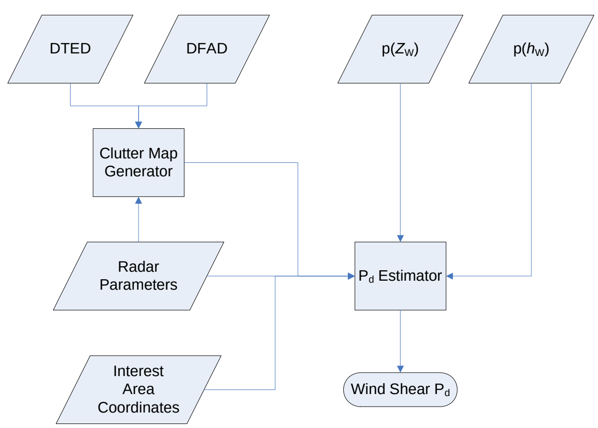

Figure 3-3. Flow chart of the radar wind-shear P_d performance estimator.

As for the probability distribution function (PDF) of the wind-shear reflectivity, $p(Z_W)$, it is based on data collected previously by the TDWR testbed radar. From these data we have direct measurements of microburst and gust-front reflectivity distributions from a site with predominantly wet microbursts (Orlando, FL) and one with a high percentage of dry microbursts (Denver, CO) (Weber and Troxel 1994). Figure 3-4 displays the observed average gust-front reflectivity PDF and both dry- and wet-site microburst PDFs. For gust fronts, the PDFs do not vary greatly with location, so we used the averaged PDF (Klingle-Wilson and Donovan 1991). For microbursts, however, the reflectivity PDF varies depending on the relative frequency of dry and wet microburst. By using the Orlando and Denver field study data as a reference we were able to generate estimates based on ancillary weather archives. Further details are given by Hallowell et al. (2008).

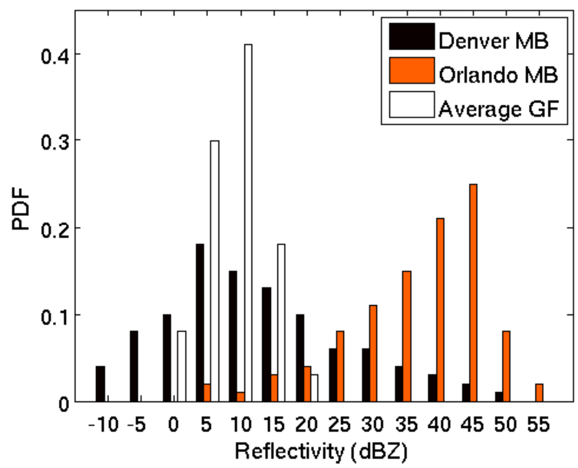

Figure 3-4. Empirical wind-shear reflectivity PDFs for microbursts (MB) and gust fronts (GF).

Empirical microburst-relative reflectivity data were not available for each airport; however, we did have an estimate of the overall reflectivity distribution at each site based on a one-year archive of 15-minute NEXRAD composite 2-km data (courtesy of Weather Services Incorporated (WSI)). A 40-km × 40-km grid of NEXRAD reflectivities was analyzed for each site and the distribution of non-zero maximum reflectivities was utilized as an indicator of microburst reflectivity tendency. NEXRAD distributions for Denver and Orlando were used to generate normalizations to the dry and wet field study profiles, respectively. Each site's NEXRAD profile was then correlated to both the Denver and Orlando NEXRAD profiles. The correlation values were in turn used to weight each site's profile between the base line (MCO and DEN) wet and dry profiles. Figure 3-5 shows the conglomeration of all the airport-specific PDF distributions color-coded according to the wet or dry tendency exhibited in the NEXRAD reflectivity data.

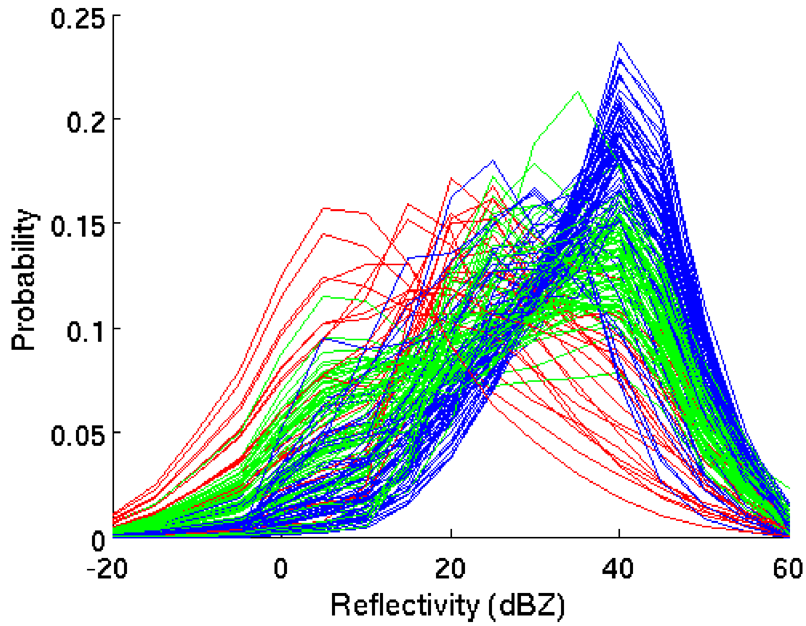

Figure 3-5. Estimated microburst reflectivity (dBZ) PDFs for all sites. The colors denote the assigned profile tendency: red is dry, blue is wet, and green is mixed.

The wind-shear outflow depth PDF, $p(h_W)$, is also an important physical parameter, as it is used in the beam-filling loss computation. Again, for gust fronts, we used a nationally averaged PDF (Wolfson et al. 1990), while for microbursts we used measured PDFs from Denver (Biron and Isaminger 1991) and Orlando (Weber et al. 1995). The cumulative distribution functions of wind-shear outflow depth for these three cases are shown in Figure 3-6. For the microburst case, we interpolated between the Denver (dry) and Orlando (wet) PDFs for each airport using a measure of a site's "microburst dryness" as a metric. This dryness scale (depicted in Figure 3-7) was based on the fraction of the estimated microburst reflectivity PDF below 20 dBZ.

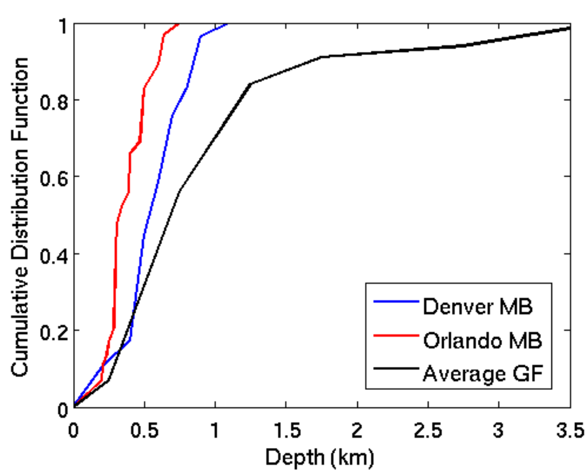

Figure 3-6. Cumulative distribution functions of wind-shear outflow depths.

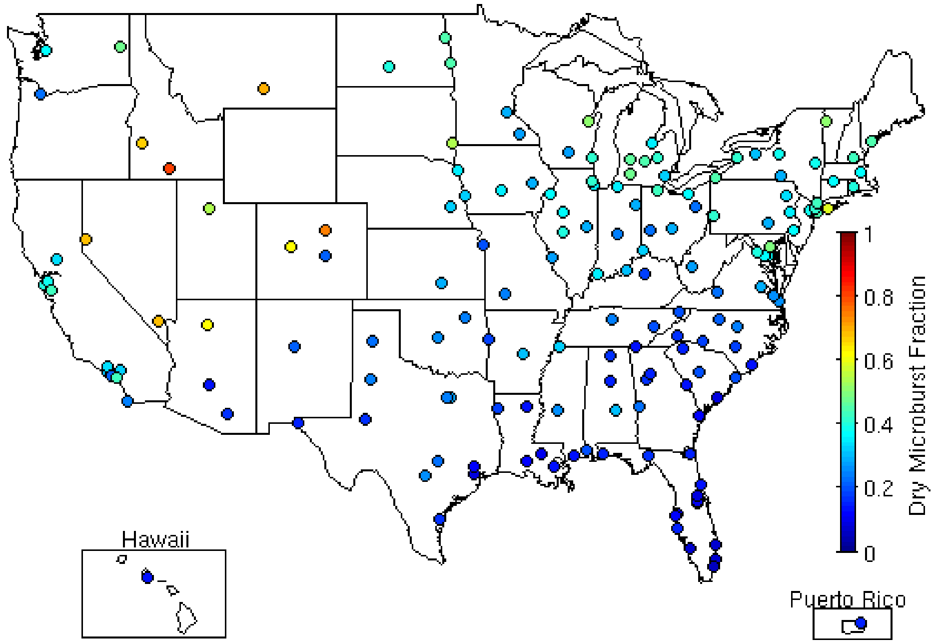

Figure 3-7. Fraction of the estimated microburst reflectivity PDF below 20 dBZ (a crude measure of the fraction of dry microbursts) for each study airport.

The process of radar wind-shear phenomenon identification can be separated into two parts. First, the radar data are processed into sequences of volumetric reflectivity and radial velocity fields. Second, a detection algorithm searches for macroscopic wind-shear signatures in these data. Likewise, we can express the radar wind-shear P_d as the product of two parts: the radar wind-shear visibility and the detection algorithm's "inherent" P_d. The visibility is the probability of pixel-level wind-shear signal being detected above noise and clutter averaged over interest area. The interest area is the union of ARENAs for microbursts and an 18-km radius around the airport for gust fronts. The detection algorithm P_d is the probability that the wind-shear phenomenon will be detected given perfect input data. From past performance analyses of the detection algorithms, we estimate values of 0.98 and 0.95 (R. Frankel, private communication) for the microburst and gust-front detection algorithms at a probability of false alarm (P_{fa}) of 0.1. We assume that all radar and lidar data will be processed by state-of-the-art detection algorithms such as the machine intelligent gust front algorithm (MIGFA) (Delanoy and Troxel, 1993).

The visibility over the interest area, A, is given by

$$Vis = \frac{\sum_A V_{RF}(\boldsymbol{r}) \Delta A(r) \sum_{Z_W = Z_{lo}(\boldsymbol{r})}^{Z_{hi}(\boldsymbol{r})} p(Z_W)}{\sum_A \Delta A(r)} , \qquad (3\text{-}1)$$

where ΔA is the incremental (pixel) area, $\boldsymbol{r}$ is the vector from the radar to ΔA, and $p(Z_W)$ is the probability distribution function of the wind-shear reflectivity Z_W (dBZ); it is normalized to sum to unity.

Note that, if we take ΔA to be the area of the radar range-azimuth resolution cell, it can be replaced by r in (3-1), since it is only proportional to the range. The first term in (3-1) is the pixel-level visibility with respect to range-fold obscuration given by

$$V_{RF}(\boldsymbol{r}) = 1 - F_{RF} F_{SCR}(\boldsymbol{r}) \ , \tag{3-2}$$

where F_{RF} is the probability of range-fold obscuration (see Appendix B), and the probability of the range-fold obscuration causing poor wind-shear velocity estimation is

$$F_{SCR}(\boldsymbol{r}) = 1 \qquad \text{for ASR-9} \tag{3-3a}$$

$$\sum_{Z_W = Z_{W,\min}}^{Z_C(\boldsymbol{r}) + SCR_{thres}} p(Z_W) \qquad \text{for other radars,} \tag{3-3b}$$

where $Z_C(\boldsymbol{r})$ (dBZ) is the clutter reflectivity and SCR_{thres} = 10 dB (Weber and Troxel 1994) is the signal-to-clutter ratio (SCR) needed for accurate velocity-shear estimation. This expression assumes the use of range-ambiguity mitigation techniques, which break down when a clutter filter is applied simultaneously. The NEXRAD upgrade utilizes systematic phase-code processing (Sachidananda and Zrnić, 1999) for this purpose, while the TDWR upgrade incorporates an adaptive approach that includes both phase-code and multiple-pulse-repetition-interval (multi-PRI) processing (Cho et al. 2005). The X-band radar will presumably use a similar method for range-alias protection. Equation (3-3) gives the probability that a clutter filter would be applied, because otherwise the SCR would be too low for good velocity estimation. The value is unity for the ASR-9, because existing range-fold protection techniques cannot be applied to its unevenly spaced pulse sequence with short coherent processing intervals (CPIs).

Z_{lo} (dBZ) is the equivalent reflectivity threshold above which the wind-shear reflectivity can be distinguished from "noise" due to such effects as clutter residue, receiver noise, partial beam filling, etc. (Figure 3-2). This quantity is calculated from

$$Z_{lo}(\boldsymbol{r}) = \frac{\max[Z_{SNR}(r), Z_{CNR}(\boldsymbol{r})] - 2BL(r)}{\delta_{LoS}(\boldsymbol{r})} \ , \tag{3-4}$$

where $\delta_{LoS}(\boldsymbol{r})$ is 1 or 0 depending on whether the radar has line-of-sight visibility to that point or not and $BL(r)$ is the beam-filling loss in dB (see Appendix B, Cho and Martin, 2007). The factor of two accounts for both the loss in signal due to partial beam filling by the desired low-altitude wind-shear signal and the increase in unwanted weather (and any other "clutter") signal in the other fraction of the beam. The beam-filling loss is dependent on the outflow depth of the wind shear phenomenon. Since we have PDFs of the outflow depths, we computed an effective loss at each range value by averaging over the PDFs.

The receiver-noise-limited component is given by

$$Z_{SNR}(r) = Z_{\min}(r) + SNR_{CPI} + SNR_{thres} \ , \tag{3-5}$$

where $Z_{min}(r)$ (dBZ) is the classical minimum detectable reflectivity, SNR_{CPI} (dB) is an adjustment factor to account for the different CPIs and pulse repetition frequencies (PRFs) used in different radars (again, see Appendix B, Cho and Martin 2007), and SNR_{thres} (dB) is the extra signal-to-noise ratio (SNR) needed for accurate velocity-shear estimation (6 dB for microburst and 3 dB for gust-front detection (Weber and Troxel 1994)).

The clutter-limited component (dBZ) is given by

$$Z_{CNR}(\boldsymbol{r}) = Z_{CREM}(\boldsymbol{r}) + SCR_{thres} \ , \tag{3-6}$$

where $Z_{CREM}(\boldsymbol{r})$ is the clutter residue map (see Appendix A).

Z_{hi} (dBZ) is the equivalent reflectivity threshold above which the wind-shear reflectivity can no longer be distinguished from noise and clutter. This limiting value is taken to be infinity except for the X-band case, where attenuation due to precipitation can be severe. For this case, we posited a simple model where the reflectivity along $\boldsymbol{r}$ is equal to the wind-shear reflectivity. With that assumption we were able to compute a Z_{hi} threshold due to precipitation attenuation. See Appendix C for details. The X-band radar was assumed to be located in the middle of the union of the ARENAs, collocated with the lidar, at a height of 8 m above the ground.

4. LIDAR PERFORMANCE ANALYSIS

The LMCT Doppler lidar (Figure 4-1) operates at a wavelength of 1.6 μm with an average transmitted power of 2 W. It has a laser beam diameter of 10 cm, a range resolution of 30 to 50 m, and a maximum scan rate of 20° s^{-1}. For a more detailed description, see Hannon (2005).

Figure 4-1. The LMCT Doppler lidar.

Lidars operate at much shorter wavelengths than radars, and the balance between scattering and attenuation relative to particles in the atmosphere is quite different. For a lidar, the maximum range occurs in the absence of large, attenuating precipitation particles, and in the presence of small aerosols that provide effective backscattering. The detection range generally decreases with increasing dBZ along the propagation path. Therefore, the summation over the wind-shear reflectivity PDF in computing the visibility was taken from $Z_{lo} = -\infty$ to

$$Z_{hi}(r) = \frac{Z_{\max}(r)}{\delta_{LoS}(\boldsymbol{r})} \ , \tag{4-1}$$

where $Z_{max}(r)$ is the maximum detectable reflectivity for the lidar. This is a simplified model of the actual physical process, because dBZ is a radar-based quantity that corresponds well to the lidar attenuation but not the backscattering strength. For our analysis, we were only concerned with two specific meteorological situations—a microburst at close range and a gust front approaching from a distance. Based on a sensitivity model that incorporated field testing data, LMCT provided us with maximum range vs. dBZ curves for the microburst case and for the gust-front case at wet and dry sites (S. Hannon, private communication). Figure 4-2 shows these curves. For the gust-front case, then, we took the average of the dry and wet range curves weighted respectively by the dryness fraction (Figure 3-7) and its complement at each site. The gust-front detection ranges are enhanced relative to the microburst detection range, because the leading edge of a gust front contains a wealth of scattering sources for the lidar, while the air mass preceding it is often quite clear. The wet-site gust front tends to have more precipitation in the vicinity of the front, so the range is reduced. A receding gust front would tend to have much more precipitation between it and the lidar, but this is a situation that is of much less importance to the safety and delay reduction missions of the terminal wind-shear sensor.

The current lidar obtains samples up to only about 12 km in range due to signal processor limitations. However, according to LMCT, it would be quite feasible to upgrade the processor to allow sampling up to 18 km in range. Therefore, as with the radars, we assumed a post-upgrade capability for the lidar.

Because the lidar beam is collimated, we assumed that it successfully avoids ground clutter altogether. The analysis, thus, is simplified relative to the radar performance estimator (see flow chart in Figure 4-3). (We did include terrain blockage for the 18-km-radius-around-the-airport gust-front P_d case, assuming a beam elevation angle of 0.7°.) These characteristics of the lidar (maximum sensitivity at low dBZ and not being affected by clutter) make the lidar an ideal complement to a radar. We also assumed that it would be sited in the center of the union of the ARENAs on an 8-m tower.

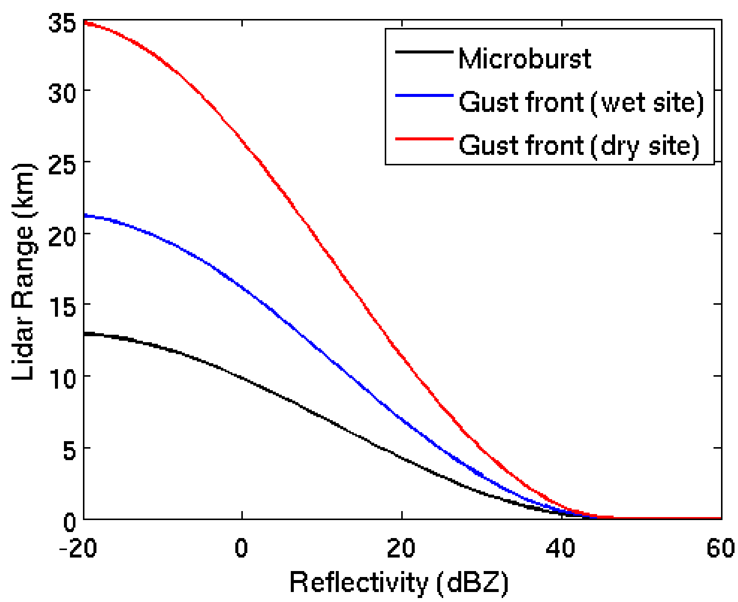

Figure 4-2. LMCT Doppler lidar maximum detection range vs. weather radar reflectivity.

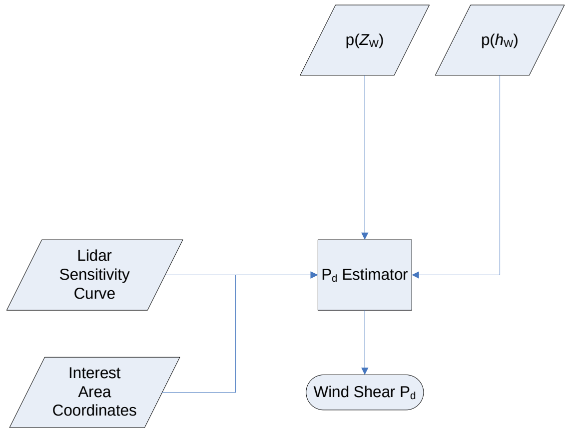

Figure 4-3. Flow chart of the lidar microburst P_d performance estimator.

5. LLWAS PERFORMANCE ANALYSIS

The LLWAS obtains its wind measurements from anemometers mounted on towers (Figure 5-1) at multiple locations in the airport vicinity. The wind-shear detection coverage provided is therefore directly dependent on the distribution of the anemometers and is limited to a small area compared to the radars and lidar. The number of sensors per airport is 6–10 for the LLWAS-RS and 8–32 for the LLWAS-NE++ (network expansion).

Figure 5-1. LLWAS tower with anemometer.

The coverage provided at each LLWAS-equipped airport is given in the data base as (nautical) miles final on arrival and departure for each runway. Since the ARENA is a one-mile-wide corridor from three miles final arrival to two miles final departure (runway inclusive), it is a simple matter to compute the LLWAS coverage as

$$Cov = \frac{\sum_{i=1}^{N_{rwy}} \left[L_{rwy}(i) + MFA(i) + MFD(i) \right]}{\sum_{i=1}^{N_{rwy}} \left[L_{rwy}(i) + 5 \right]} \, , \qquad (5\text{-}1)$$

where N_{rwy} is the number of runways, L_{rwy} is the runway length, MFA is the miles final arrival covered, and MFD is the miles final departure covered. The microburst P_d is then estimated as the product of Cov and the LLWAS detection algorithm P_d, which we took to be 0.97 (at P_{fa} = 0.1) (Wilson and Cole 1993).

To verify the accuracy of the data base, we ran the NCAR code (courtesy of W. Wilson) originally used in the development of the LLWAS microburst detection algorithm to compute the coverage at Orlando (MCO) with the actual airport configuration file (ACF) ingested by LLWAS. The data base coverage using (5-1) yielded 87% while the NCAR code with ACF gave 88% coverage, an excellent agreement.

6. SENSOR COMBINATION ANALYSIS

Fusion of data from multiple sensors has the potential to increase wind-shear detection probability. At the minimum, holes in the coverage of one sensor due to blockage, clutter residue, lack of sensitivity, etc. may be filled in by another sensor with better sensing conditions in those areas. Line-of-sight velocity fields cannot be directly merged for non-collocated sensors, but sophisticated detection algorithms that perform fuzzy logic operations on interest fields would allow merging at that level instead of at the base data level. Therefore, for radar + radar and radar(s) + lidar combinations, we computed the visibility pixel-by-pixel (the summand associated with each $\boldsymbol{r}$ location in (3-1)) for each sensor and took the greater value before summing over interest region A. However, current plans for the lidar addition to the TDWR at Las Vegas call for integration at the wind-shear message level, so our model results for that site may well overestimate the actual performance achieved. Integration at the pixel level is an ideal that exposes the full potential of what a combination of two remote sensing instruments could provide for wind-shear detection.

In the case of radar(s) + LLWAS, the detection phenomenologies are independent of each other. The data on which the detection algorithms work are quite different—volumetric base data for the radar and point measurements of surface winds for the LLWAS—so they cannot be fused together in the same way as the radar and lidar data. In practice, the detection alert is issued after combining the wind-shear message outputs from the two systems (Cole 1992). Thus, we took the P_d for each sensor and combined them as $P_d(\text{combined}) = 1 - [1 - P_d(\text{radar})][1 - P_d(\text{LLWAS})]$. In theory, the false alarm rates also combine to increase in similar fashion. However, clever use of all the available contextual data can reduce false alarms (Cole and Todd 1996) so we assumed that the P_{fa} stayed constant.

7. RESULTS

Here we give the airport-specific wind-shear detection probability estimates for single sensors and sensor combinations. Results are given for post-upgrade performance characteristics in the case of the TDWR, ASR-9 WSP, and NEXRAD. (For comparison purposes, single-radar results for the "legacy" systems are given at the end.) The false-alarm probability is nominally 10% throughout. A color code is used for the microburst results with green for $P_d \geq 90\%$, yellow for $80\% \leq P_d < 90\%$, and red for $P_d < 80\%$, which are keyed to the FAA requirement of 90% detection rate. No color code is used for the gust-front results, since there is no specific FAA requirement.

Table 7-1 gives the single-radar results for the TDWR airports. The post-upgrade TDWR is expected to meet the microburst detection requirement at all airports, except for Las Vegas (LAS) due to the severe road clutter there. For gust-front coverage within the 18-km-radius interest area, the TDWR also does very well except for Las Vegas, Phoenix (PHX), and Salt Lake City (SLC). Since the gust-front reflectivity PDF used was the same for every airport, the poor performance at these three airports are due to terrain blockage and clutter, and not due to the dryness of the sites. This conclusion is reinforced by the high P_ds at Denver, which is the fourth "dry" site.

The potential WSP, as expected, would not perform as well as the TDWR. The reduction in capability is more pronounced for gust fronts. On average, the loss in detection probability relative to the TDWR is 9 percentage points for the microburst case and 24 percentage points for the gust front case. There is no ASR-9 at five airports (DAL, LGA, MDW, PBI, and SJU) and WSPs installed at the closest ones would not yield adequate capability at those sites. Unlike with the TDWR, the dry-site microburst reflectivity PDFs do have a significant negative impact on detection probability as can be seen from the Denver results. This is due to the much lower sensitivity of the ASR-9.

The NEXRAD would yield performance comparable to the TDWR if located close enough to the airport, which is the case for less than half of the TDWR airports. (Also, we note again that the current operational NEXRAD scan update rates are not fast enough for microburst detection.)

The performance of the proposed LMCT X-band radar falls between that of the TDWR and WSP in general. Site-specific results for the X-band system should be taken with a grain of salt, since the assumed siting at the center of the union of the ARENAs with a tower height of 8 m is neither optimized nor known to be feasible. Actual siting will have an effect on the P_ds for better or for worse. For example, the extremely poor performance in Pittsburgh (PIT) indicates that a more careful siting analysis is needed before a new radar is placed there.

TABLE 7-1

Single-Radar Wind-Shear Detection Probability (%) at TDWR Airports

Airport	Microburst				Gust Front			
	TDWR	WSP	NEXRAD	X-band	TDWR	WSP	NEXRAD	X-band
ADW	95	81	75	87	92	72	64	89
ATL	96	91	97	94	91	66	93	88
BNA	98	89	94	95	93	67	85	91
BOS	97	89	80	94	93	80	77	91
BWI	96	74	0	84	90	68	5	85
CLE	97	90	96	96	94	79	89	94
CLT	97	90	0	91	91	68	0	90
CMH	98	89	0	94	94	69	0	90
CVG	97	88	0	94	94	76	0	92
DAL	96	41	68	94	91	32	50	91
DAY	97	91	5	96	93	69	30	92
DCA	97	84	87	88	90	74	74	69
DEN	96	60	93	93	95	75	92	94
DFW	97	88	91	96	93	67	91	91
DTW	98	89	0	96	94	79	0	95
EWR	96	85	0	95	85	78	0	87
FLL	97	96	94	96	87	62	57	85
HOU	97	94	96	96	89	53	82	84
IAD	97	81	85	88	91	69	75	86
IAH	97	92	76	93	89	52	52	72
ICT	97	89	93	94	92	70	80	89
IND	96	93	96	96	94	77	88	94
JFK	97	86	0	95	92	80	0	94
LAS	85	69	0	62	57	59	0	58
LGA	97	27	0	95	94	39	0	93
MCI	98	95	13	96	94	82	32	95
MCO	98	96	0	96	91	70	18	92
MDW	98	23	93	96	94	37	95	94
MEM	98	84	96	92	92	61	89	89
MIA	95	92	96	96	86	52	76	82
MKE	97	79	14	91	94	65	41	93
MSP	97	91	95	96	95	79	93	94
MSY	96	93	60	93	89	58	50	87
OKC	97	92	96	96	92	76	88	92
ORD	96	82	73	92	92	66	94	89
PBI	95	0	0	96	89	0	0	85
PHL	93	78	0	90	86	57	5	80
PHX	94	89	95	94	58	57	89	63
PIT	97	85	97	19	95	78	94	27
RDU	97	87	91	87	92	65	85	88
SDF	97	82	95	89	92	60	89	77
SJU	97	0	0	94	84	0	0	74
SLC	93	74	0	89	65	55	0	69
STL	97	90	96	95	94	81	94	95
TPA	96	96	98	97	85	80	93	93
TUL	97	89	97	93	92	69	93	88
Median	97	88	83	94	92	68	75	89

Table 7-2 gives the single-radar results for the WSP airports. Here the fraction of NEXRADs close enough to the airport to be useful is even smaller than for the TDWR airports. The results for Honolulu (HNL) may be slightly overestimated, because no DFAD data was available (i.e., no road clutter information) for this site. The poor performance of the WSP at AUS appears to be due to strong clutter within the ARENAs as the terrain slopes up away from the radar to the west.

TABLE 7-2

Single-Radar Wind-Shear Detection Probability (%) at WSP Airports

Airport	Microburst			Gust Front		
	WSP	NEXRAD	X-band	WSP	NEXRAD	X-band
ABQ	93	97	96	68	77	76
ALB	88	0	93	78	0	90
AUS	73	0	95	53	18	90
BDL	90	0	93	80	0	77
BHM	91	96	48	66	94	16
BUF	90	97	96	79	89	94
CHS	93	0	94	49	0	75
CID	92	0	95	77	0	92
DSM	88	95	94	75	89	94
ELP	94	3	96	69	32	79
FWA	88	7	94	74	29	91
GEG	86	93	93	77	85	86
GRR	90	97	96	80	93	95
GSO	92	0	72	70	0	75
HNL	96	0	92	56	0	61
HPN	90	0	93	81	15	85
HSV	94	0	92	72	0	87
ISP	79	95	94	77	90	92
JAX	84	97	96	67	90	94
LAX	85	0	93	60	0	78
LBB	92	96	96	74	86	94
MDT	82	0	85	61	0	29
MSN	86	0	92	71	22	92
ONT	91	0	94	60	0	66
ORF	83	0	89	52	4	82
PDX	91	0	80	69	0	32
RIC	83	42	87	56	43	78
ROC	93	0	96	81	0	95
SAT	92	89	96	77	94	94
SEA	87	0	94	72	0	84
SRQ	97	97	96	81	95	94
SYR	84	0	91	72	0	89
TOL	79	0	87	64	0	86
TUS	88	0	95	57	0	84
TYS	93	0	27	73	0	36
Median	90	0	94	72	4	86

Table 7-3 gives the single-radar results for the LLWAS-RS airports. WSPs were not considered for these sites, because there are no ASR-9s located at these airports.

TABLE 7-3

Single-Radar Wind-Shear Detection Probability (%) at LLWAS-RS Airports

Airport	Microburst		Gust Front	
	NEXRAD	X-band	NEXRAD	X-band
AGS	0	91	0	71
AVL	0	88	0	32
BIL	92	66	88	79
BTR	0	94	0	80
CAE	92	50	72	42
CHA	0	79	0	45
COS	79	82	57	65
CRW	96	64	87	56
CSG	0	88	0	83
DAB	0	94	0	87
FAY	0	93	0	82
FSD	88	92	90	93
FSM	97	93	87	93
GRB	93	90	79	90
GSP	97	94	82	89
JAN	95	88	84	87
LAN	0	92	4	93
LEX	0	95	0	94
LIT	97	92	88	87
LNK	58	95	51	94
MAF	96	95	83	90
MGM	0	93	9	89
MLI	93	84	84	68
MLU	0	94	0	74
MOB	95	94	80	88
OMA	90	94	88	64
PIA	23	91	38	89
PNS	0	95	0	83
PVD	89	95	95	94
ROA	0	80	0	36
RST	0	95	0	93
RSW	0	95	0	94
SAV	16	91	36	71
SFO	0	79	0	48
SGF	97	95	84	93
SHV	96	93	79	92
SPI	60	96	91	94
SUX	0	92	0	90
TLH	93	91	62	78
TRI	0	76	0	57
Median	41	92	44	85

Table 7-4 gives the single-radar results for the other 41 airports. Preexisting TDWRs are close enough to four airports to provide satisfactory wind-shear detection capability (MCO for ORL and SFB, ATL for PDK, and TPA for PIE). Two airports (BUR and OAK) have ASR-9s on site on which WSPs can be installed; however, both project to have marginal performance. All other airports do not have an ASR-9 located close enough. Only a few airports have NEXRADs close enough for adequate wind-shear coverage.

TABLE 7-4

Single-Radar Wind-Shear Detection Probability (%) at Other Airports

Airport	Microburst				Gust Front			
	TDWR	WSP	NEXRAD	X-band	TDWR	WSP	NEXRAD	X-band
ABE	0	0	0	95	0	0	0	83
AMA	0	0	97	95	0	0	88	92
ASE	0	0	0	50	0	0	0	3
AVP	0	0	0	74	0	0	0	29
AZO	0	0	0	95	0	0	18	94
BGM	0	0	97	96	0	0	93	94
BIS	0	0	92	92	0	0	84	88
BOI	0	0	98	88	0	0	75	56
BTV	0	0	94	92	0	0	70	73
BUR	0	77	0	78	0	42	0	38
CAK	75	0	32	96	52	0	42	92
CMI	0	0	0	96	0	0	0	94
CRP	0	0	97	96	0	0	90	94
ERI	0	0	0	84	0	0	0	67
EVV	0	0	0	95	0	0	0	95
FAR	0	0	0	89	0	0	0	92
FNT	0	0	52	95	0	0	72	93
GCN	0	0	0	92	0	0	0	78
GFK	0	0	38	95	0	0	69	94
GPT	0	0	0	95	0	0	6	82
ILM	0	0	76	93	0	0	55	72
LFT	0	0	0	95	0	0	0	87
LGB	0	52	0	88	0	31	0	69
MBS	0	0	0	94	0	0	0	88
MHT	0	40	0	95	0	49	0	76
MYR	0	0	82	87	0	0	55	72
OAK	0	83	0	91	0	58	0	64
ORL	95	46	0	93	91	37	1	83
PDK	98	4	77	95	92	9	54	88
PHF	0	0	85	86	0	1	77	81
PIE	97	48	98	96	88	43	94	83
PWM	0	0	65	95	0	27	95	94
RNO	0	0	0	65	0	0	0	16
SAN	0	0	0	89	0	26	0	53
SBN	0	0	0	93	0	0	14	88
SFB	98	0	0	96	82	0	0	76
SJC	0	54	0	89	0	37	0	56
SMF	0	20	96	96	0	33	85	89
SNA	0	17	0	87	0	27	0	65
TWF	0	0	0	89	0	0	0	74
Median	0	0	0	93	0	0	1	83

Table 7-5 gives the lidar results for all airports. Clearly, the lidar by itself is not sufficient for acceptable terminal wind-shear detection performance. However, we will see that it is an excellent complement to a radar. Note the tendency for better performance at the drier sites. Also, the smaller the ARENAs are, the better the chance for microburst coverage and detection probability.

TABLE 7-5
Lidar Wind-Shear Detection Probability (%) at All Airports

Airport	MB	GF	Airport	MB	GF	Airport	MB	GF	Airport	MB	GF
ADW	39	65	ABQ	19	50	AGS	16	47	ABE	37	58
ATL	16	53	ALB	41	64	AVL	23	23	AMA	22	57
BNA	24	58	AUS	23	57	BIL	66	68	ASE	63	3
BOS	35	63	BDL	37	55	BTR	15	50	AVP	35	22
BWI	48	73	BHM	18	12	CAE	22	26	AZO	49	72
CLE	37	66	BUF	43	68	CHA	17	28	BGM	32	61
CLT	19	53	CHS	12	49	COS	22	44	BIS	42	65
CMH	31	60	CID	31	61	CRW	30	36	BOI	64	52
CVG	30	62	DSM	36	64	CSG	26	57	BTV	51	59
DAL	28	59	ELP	18	47	DAB	16	51	BUR	37	33
DAY	24	57	FWA	30	61	FAY	21	54	CAK	25	57
DCA	38	50	GEG	47	69	FSD	52	75	CMI	29	60
DEN	62	84	GRR	44	71	FSM	22	39	CRP	22	53
DFW	21	58	GSO	24	56	GRB	50	73	ERI	47	53
DTW	29	62	HNL	14	39	GSP	22	52	EVV	36	64
EWR	39	64	HPN	45	44	JAN	30	59	FAR	44	70
FLL	10	47	HSV	19	51	LAN	45	70	FNT	42	68
HOU	12	49	ISP	54	77	LEX	21	54	GCN	61	69
IAD	35	67	JAX	18	52	LIT	30	61	GFK	45	70
IAH	12	51	LAX	32	62	LNK	31	62	GPT	16	51
ICT	30	61	LBB	26	58	MAF	19	53	ILM	17	51
IND	25	61	MDT	33	19	MGM	33	62	LFT	15	50
JFK	40	70	MSN	28	59	MLI	36	49	LGB	22	48
LAS	59	60	ONT	34	47	MLU	16	51	MBS	37	64
LGA	42	67	ORF	30	59	MOB	22	55	MHT	44	59
MCI	20	55	PDX	25	26	OMA	32	43	MYR	23	55
MCO	12	50	RIC	30	61	PIA	37	62	OAK	40	51
MDW	37	64	ROC	31	61	PNS	18	46	ORL	15	49
MEM	27	62	SAT	29	59	PVD	42	67	PDK	18	52
MIA	8	47	SEA	39	59	ROA	26	31	PHF	29	59
MKE	40	68	SRQ	18	52	RST	30	60	PIE	14	50
MSP	28	60	SYR	40	66	RSW	12	48	PWM	47	71
MSY	15	51	TOL	43	68	SAV	16	51	RNO	66	20
OKC	24	59	TUS	18	51	SFO	40	39	SAN	28	35
ORD	37	68	TYS	24	46	SGF	26	57	SBN	37	64
PBI	11	48	Median	30	58	SHV	23	55	SFB	12	49
PHL	36	65				SPI	40	67	SJC	44	59
PHX	20	43				SUX	36	64	SMF	37	64
PIT	38	21				TLH	18	53	SNA	48	58
RDU	25	57				TRI	22	35	TWF	79	71
SDF	30	58				Median	24	53	Median	37	58
SJU	19	50									
SLC	48	64									
STL	27	59									
TPA	12	49									
TUL	25	58									
Median	28	59									

Table 7-6 gives the LLWAS results for the LLWAS-RS airports (left side) and LLWAS-NE++ airports (right side). The detection performance is determined by the area covered. Only Denver (DEN) has enough anemometers installed to cover all of the ARENAs for microburst detection. For the 18-km-radius interest area of gust fronts, the LLWAS is virtually useless.

TABLE 7-6
LLWAS Wind-Shear Detection Probability (%) at LLWAS-RS/NE++ Airports

Airport	Microburst	Gust Front	Airport	Microburst	Gust Front
AGS	46	1	ATL	62	1
AVL	43	1	DEN	97	12
BIL	62	2	DFW	62	1
BTR	43	1	LGA	40	2
CAE	47	1	MCO	85	7
CHA	53	1	MSY	31	2
CSG	64	2	ORD	76	9
COS	52	2	STL	44	3
CRW	44	1	TPA	60	4
DAB	57	2	Median	62	5
FAY	45	1			
FSD	47	2			
FSM	49	1			
GRB	47	1			
GSP	47	1			
JAN	59	1			
LAN	48	2			
LEX	47	1			
LIT	58	2			
LNK	62	2			
MAF	53	2			
MBM	41	1			
MLI	55	2			
MLU	54	2			
MOB	49	1			
OMA	47	1			
PIA	48	1			
PNS	46	1			
PVD	53	2			
ROA	53	2			
RST	43	1			
RSW	48	1			
SAV	51	1			
SFO	55	2			
SGF	43	1			
SHV	50	1			
SPI	44	2			
SUX	58	2			
TLH	50	1			
TRI	49	1			
Median	49	1			

Table 7-7 gives the lidar + radar results for the TDWR airports. For microburst detection, the lidar + TDWR combination exceeds 90% detection probability at all airports. The same is true for lidar + WSP except for the five airports where the ASR-9 is not on site. Lidar + X-band does just as well. For gust fronts, there are a few sites that present blockage issues. Overall, we see that a lidar + radar combination provides superior terminal wind-shear detection capability.

TABLE 7-7
Lidar + Radar Wind-Shear Detection Probability (%) at TDWR Airports

Airport	Microburst				Gust Front			
	TDWR	WSP	NEXRAD	X-band	TDWR	WSP	NEXRAD	X-band
ADW	98	97	97	96	94	89	83	94
ATL	97	95	98	96	94	83	94	93
BNA	98	95	97	97	94	85	93	94
BOS	98	98	98	96	94	90	86	94
BWI	98	96	48	97	94	93	73	94
CLE	98	97	97	97	95	90	94	95
CLT	98	97	97	97	93	82	53	94
CMH	98	97	31	97	94	86	60	95
CVG	98	97	30	97	95	89	62	95
DAL	97	68	85	97	94	73	77	94
DAY	98	97	29	97	94	85	71	94
DCA	98	96	98	95	92	87	85	87
DEN	98	92	98	97	95	93	95	95
DFW	98	95	98	97	94	83	92	94
DTW	98	97	29	97	95	89	62	95
EWR	97	97	39	97	90	90	64	91
FLL	97	97	97	97	92	81	74	93
HOU	97	95	97	96	93	75	89	92
IAD	98	95	95	96	94	90	92	94
IAH	97	94	81	96	92	74	74	87
ICT	98	97	96	96	94	87	92	94
IND	97	96	96	97	95	87	92	94
JFK	98	97	40	97	94	92	70	95
LAS	96	95	59	83	65	79	60	77
LGA	98	69	42	97	95	78	67	95
MCI	98	97	32	97	95	88	70	95
MCO	98	97	32	97	93	82	63	94
MDW	98	60	98	97	95	77	95	95
MEM	98	93	97	96	94	87	94	95
MIA	96	94	96	96	92	77	89	92
MKE	98	97	53	97	95	88	80	95
MSP	98	97	98	97	95	88	94	95
MSY	97	96	67	96	93	79	73	94
OKC	98	97	98	97	94	88	93	95
ORD	98	95	91	97	94	88	95	94
PBI	96	11	11	97	93	48	48	93
PHL	97	95	36	97	93	86	69	92
PHX	96	94	98	96	73	76	93	77
PIT	98	96	98	48	95	81	94	42
RDU	98	96	95	94	94	84	92	94
SDF	98	95	98	96	94	84	93	90
SJU	97	19	19	95	88	50	50	86
SLC	97	95	48	97	86	78	64	79
STL	98	96	98	97	95	89	95	95
TPA	97	97	98	97	91	86	94	95
TUL	98	97	98	96	94	87	94	94
Median	98	96	96	97	94	86	85	94

Table 7-8 gives the lidar + radar results for the WSP airports. Again, the microburst detection probability is nearly uniformly excellent for WSP and X-band, while the gust-front results vary more widely.

TABLE 7-8

Lidar + Radar Wind-Shear Detection Probability (%) at WSP Airports

Airport	Microburst			Gust Front		
	WSP	NEXRAD	X-band	WSP	NEXRAD	X-band
ABQ	97	98	97	80	78	82
ALB	98	41	96	90	64	94
AUS	86	23	97	76	68	94
BDL	98	37	95	90	55	88
BHM	96	98	57	72	94	30
BUF	97	97	97	91	94	95
CHS	96	12	96	72	49	88
CID	98	31	97	87	61	94
DSM	97	97	97	89	94	95
ELP	97	20	97	82	70	86
FWA	97	37	97	88	73	94
GEG	98	98	97	91	93	93
GRR	98	98	97	93	95	95
GSO	97	24	79	86	56	88
HNL	97	14	93	67	39	66
HPN	98	45	95	86	74	92
HSV	97	19	94	84	51	92
ISP	97	98	97	94	94	95
JAX	89	98	97	79	93	95
LAX	95	32	97	83	62	89
LBB	97	97	96	86	92	95
MDT	94	33	89	65	19	38
MSN	96	28	96	87	71	94
ONT	97	34	96	77	47	77
ORF	95	30	96	80	63	93
PDX	96	25	85	76	26	46
RIC	96	67	96	81	76	91
ROC	98	31	97	89	61	95
SAT	97	98	97	88	95	95
SEA	96	39	97	86	59	90
SRQ	97	98	97	87	95	95
SYR	97	40	97	88	66	93
TOL	97	43	96	88	68	94
TUS	92	18	96	77	51	91
TYS	97	24	46	84	46	68
Median	97	37	97	86	68	93

Table 7-9 gives the lidar + radar results for the LLWAS-RS airports.

TABLE 7-9

Lidar + Radar Wind-Shear Detection Probability (%) at LLWAS-RS Airports

Airport	Microburst		Gust Front	
	NEXRAD	X-band	NEXRAD	X-band
AGS	16	94	47	87
AVL	23	93	23	48
BIL	97	86	92	93
BTR	15	96	50	90
CAE	95	64	80	56
CHA	17	83	28	63
COS	90	85	64	71
CRW	97	74	92	67
CSG	26	96	57	93
DAB	16	96	51	93
FAY	21	96	54	90
FSD	97	97	95	95
FSM	97	96	90	83
GRB	97	97	92	95
GSP	97	96	89	93
JAN	97	96	91	94
LAN	45	97	72	95
LEX	21	96	54	95
LIT	97	96	93	94
LNK	80	97	79	95
MAF	97	96	90	93
MGM	33	96	68	94
MLI	97	92	84	80
MLU	16	96	51	88
MOB	97	96	90	94
OMA	98	96	88	66
PIA	58	97	78	93
PNS	18	96	46	83
PVD	98	97	95	95
ROA	26	85	31	56
RST	30	97	60	95
RSW	12	96	48	95
SAV	31	96	69	87
SFO	40	88	39	63
SGF	97	97	92	95
SHV	97	96	88	95
SPI	90	97	92	95
SUX	36	97	64	94
TLH	95	96	83	92
TRI	22	81	35	76
Median	69	96	75	93

Table 7-10 gives the lidar + radar results for the other airports. With the lidar the WSP at BUR and OAK projects to meet the microburst detection requirement.

TABLE 7-10
Lidar + Radar Wind-Shear Detection Probability (%) at Other Airports

Airport	Microburst				Gust Front			
	TDWR	WSP	NEXRAD	X-band	TDWR	WSP	NEXRAD	X-band
ABE	37	37	37	97	58	58	58	90
AMA	22	22	97	96	57	57	93	95
ASE	63	63	63	80	3	3	3	3
AVP	35	35	35	83	22	22	22	42
AZO	49	49	49	97	72	72	79	95
BGM	32	32	98	97	61	61	94	95
BIS	42	42	96	97	65	65	93	94
BOI	64	64	98	96	52	52	88	67
BTV	51	51	97	96	59	59	83	83
BUR	37	95	37	87	33	56	33	52
CAK	86	25	53	97	76	57	74	94
CMI	29	29	29	97	60	60	60	95
CRP	22	22	97	97	53	53	93	95
ERI	47	47	47	95	53	53	53	78
EVV	36	36	36	97	64	64	64	95
FAR	44	44	44	97	70	70	70	95
FNT	42	42	90	97	68	68	85	95
GCN	61	61	61	97	69	69	69	82
GFK	45	45	82	97	70	70	85	95
GPT	16	16	16	96	51	51	57	91
ILM	17	17	83	96	51	51	75	88
LFT	15	15	15	96	50	50	50	94
LGB	22	73	22	93	48	48	48	85
MBS	37	37	37	97	64	64	64	93
MHT	44	82	44	97	59	81	59	85
MYR	23	23	93	95	55	55	76	89
OAK	40	95	40	97	51	77	51	71
ORL	96	60	15	96	94	68	50	93
PDK	98	22	87	97	94	60	75	94
PHF	29	29	98	96	59	60	84	93
PIE	97	62	98	97	92	69	94	91
PWM	47	47	96	97	71	79	95	95
RNO	66	66	66	90	20	20	20	25
SAN	28	38	28	94	35	69	35	60
SBN	37	37	37	97	64	64	72	94
SFB	98	12	12	97	84	49	49	88
SJC	44	83	44	96	59	59	59	73
SMF	37	56	97	97	64	75	92	94
SNA	48	64	48	97	58	58	58	83
TWF	79	79	79	97	71	71	71	89
Median	42	42	49	97	59	60	69	91

Table 7-11 gives the NEXRAD + radar and NEXRAD + radar + lidar results for the TDWR airports. In practical terms, an interesting question is which airports would benefit most from having NEXRAD data in addition to the TDWR data in detecting gust fronts. (Recall that the NEXRAD currently does not have an update rate fast enough for timely microburst detection.) Comparing with the results in Table 7-1, we see that PHX and TPA could improve their gust-front detection performance significantly if the NEXRAD data were to be fused with the TDWR data at the interest field level.

TABLE 7-11

NEXRAD + Radar/Lidar Wind-Shear Detection Probability (%) at TDWR Airports

Airport	Microburst				Gust Front			
	TDWR	WSP	TDWR + Lidar	WSP + Lidar	TDWR	WSP	TDWR + Lidar	WSP + Lidar
ADW	96	85	98	98	94	86	95	92
ATL	98	97	98	98	95	94	95	94
BNA	98	96	98	98	94	91	95	94
BOS	97	89	98	98	94	89	95	93
BWI	96	74	98	96	90	68	94	93
CLE	98	97	98	98	95	93	95	94
CLT	97	90	98	97	91	68	93	82
CMH	98	89	98	97	94	69	94	86
CVG	97	88	98	97	94	76	95	89
DAL	96	76	98	91	93	57	95	81
DAY	97	91	98	97	93	78	94	89
DCA	97	90	98	98	94	91	95	93
DEN	96	94	98	98	95	94	95	95
DFW	97	93	98	98	95	93	95	94
DTW	98	89	98	97	94	79	95	89
EWR	96	85	97	97	85	78	90	90
FLL	98	97	98	98	91	81	94	88
HOU	98	98	98	98	93	88	94	92
IAD	97	91	98	97	92	84	95	94
IAH	98	96	98	98	92	76	93	84
ICT	98	95	98	98	94	88	95	94
IND	98	97	98	97	95	91	95	93
JFK	97	86	98	97	92	80	94	92
LAS	85	69	96	95	57	59	65	79
LGA	97	27	98	69	94	39	95	78
MCI	98	95	98	97	95	85	95	91
MCO	98	96	98	97	91	72	93	83
MDW	98	93	98	98	95	95	95	95
MEM	98	97	98	98	94	92	95	95
MIA	98	98	98	98	91	83	94	92
MKE	97	79	98	97	95	77	95	90
MSP	97	96	98	98	95	94	95	95
MSY	97	95	98	97	92	77	94	87
OKC	98	97	98	98	93	93	95	94
ORD	97	86	98	96	95	94	95	95
PBI	95	0	96	11	89	0	93	48
PHL	93	78	97	95	87	60	94	88
PHX	97	96	98	98	92	92	94	94
PIT	98	98	98	98	95	94	95	95
RDU	98	95	98	98	94	91	95	94
SDF	98	95	98	98	94	92	95	94
SJU	97	0	97	19	84	0	88	50
SLC	93	74	97	95	65	55	86	78
STL	98	96	98	98	95	95	95	95
TPA	98	98	98	98	94	94	95	95
TUL	98	97	98	98	95	94	95	95
Median	97	93	98	98	94	86	95	92

Table 7-12 gives the NEXRAD + radar and NEXRAD + radar + lidar results for the WSP airports. The WSP, with its gust-front detection performance generally much lower than that of the TDWR, correspondingly benefits more from having NEXRAD data available. Comparing with the results in Table 7-2, we see that 14 airports have 10 or more percentage point increases in gust-front detection probability when the NEXRAD data are fused with the WSP data.

TABLE 7-12

NEXRAD + WSP/Lidar Wind-Shear Detection Probability (%) at WSP Airports

Airport	Microburst		Gust Front	
	WSP	WSP + Lidar	WSP	WSP + Lidar
ABQ	97	98	86	88
ALB	88	98	78	90
AUS	73	86	66	84
BDL	90	98	80	90
BHM	96	98	94	94
BUF	97	98	92	94
CHS	93	96	49	72
CID	92	98	77	87
DSM	96	98	93	95
ELP	94	97	79	89
FWA	88	97	78	90
GEG	96	98	91	94
GRR	98	98	94	95
GSO	92	97	70	86
HNL	96	97	56	67
HPN	90	98	84	89
HSV	94	97	72	84
ISP	95	98	93	95
JAX	98	98	93	94
LAX	85	95	60	83
LBB	97	98	91	94
MDT	82	94	61	65
MSN	86	96	75	89
ONT	91	97	60	77
ORF	83	95	54	81
PDX	91	96	69	76
RIC	85	97	72	87
ROC	93	98	81	89
SAT	93	98	94	95
SEA	87	96	72	86
SRQ	98	98	95	95
SYR	84	97	72	88
TOL	79	97	64	88
TUS	88	92	57	77
TYS	93	97	73	84
Median	92	97	77	88

Table 7-13 gives the NEXRAD + radar and NEXRAD + radar + lidar results for the other airports.

TABLE 7-13

NEXRAD + Radar/Lidar Wind-Shear Detection Probability (%) at Other Airports

Airport	Microburst				Gust Front			
	TDWR	WSP	TDWR + Lidar	WSP + Lidar	TDWR	WSP	TDWR + Lidar	WSP + Lidar
ABE	0	0	37	37	0	0	58	58
AMA	97	97	97	97	88	88	93	93
ASE	0	0	63	63	0	0	3	3
AVP	0	0	35	35	0	0	22	22
AZO	0	0	49	49	18	18	79	79
BGM	97	97	98	98	93	93	94	94
BIS	92	92	96	96	84	84	93	93
BOI	98	98	98	98	75	75	88	88
BTV	94	94	97	97	70	70	83	83
BUR	0	77	37	95	0	42	33	56
CAK	75	32	86	53	53	42	76	74
CMI	0	0	29	29	0	0	60	60
CRP	97	97	97	97	90	90	93	93
ERI	0	0	47	47	0	0	53	53
EVV	0	0	36	36	0	0	64	64
FAR	0	0	44	44	0	0	70	70
FNT	52	52	90	90	72	72	85	85
GCN	0	0	61	61	0	0	69	69
GFK	38	38	82	82	69	69	85	85
GPT	0	0	16	16	6	6	57	57
ILM	76	76	83	83	55	55	75	75
LFT	0	0	15	15	0	0	50	50
LGB	0	52	22	73	0	31	48	48
MBS	0	0	37	37	0	0	64	64
MHT	0	40	44	82	0	49	59	81
MYR	82	82	93	93	55	55	76	76
OAK	0	83	40	95	0	58	51	77
ORL	95	46	96	60	91	37	94	68
PDK	98	77	98	87	94	54	95	75
PHF	85	85	98	98	77	77	84	85
PIE	98	98	98	98	95	94	95	95
PWM	65	65	96	96	95	95	95	95
RNO	0	0	66	66	0	0	20	20
SAN	0	11	28	38	0	26	35	69
SBN	0	0	37	37	14	14	72	72
SFB	98	0	98	12	82	0	84	49
SJC	0	54	44	83	0	37	59	59
SMF	96	96	97	97	85	88	92	93
SNA	0	17	48	64	0	27	58	58
TWF	0	0	79	79	0	0	71	71
Median	0	38	63	73	14	37	71	71

Table 7-14 gives the LLWAS + radar(s) results for the TDWR airports. The LLWAS + TDWR combination exceeds 90% detection probability at all airports. LLWAS + X-band does just as well except at LAS and PIT. The LLWAS + WSP combination exceeds 90% detection probability at 36 out of 46 airports.

TABLE 7-14

LLWAS + Radar(s) Microburst Detection Probability (%) at TDWR Airports

Airport	TDWR	WSP	NEXRAD	X-band	NEXRAD + TDWR	NEXRAD + WSP
ADW	98	91	87	93	98	92
ATL	99	96	99	98	99	99
BNA	99	94	97	98	99	98
BOS	98	94	90	97	98	95
BWI	98	87	49	92	98	87
CLE	98	95	98	98	99	99
CLT	99	95	49	95	99	95
CMH	99	94	49	97	99	94
CVG	99	94	49	97	99	94
DAL	98	70	84	97	98	87
DAY	99	95	51	98	99	95
DCA	98	92	93	94	99	95
DEN	100	99	100	100	100	100
DFW	99	95	97	98	99	97
DTW	99	94	49	98	99	94
EWR	98	92	49	97	98	92
FLL	98	98	97	98	99	99
HOU	99	97	98	98	99	99
IAD	98	90	92	94	98	95
IAH	98	96	88	96	99	98
ICT	99	94	96	97	99	97
IND	98	96	98	98	99	98
JFK	98	93	49	98	98	93
LAS	92	84	49	80	92	84
LGA	98	56	40	97	98	56
MCI	99	97	56	98	99	97
MCO	100	99	85	99	100	99
MDW	99	61	97	98	99	97
MEM	99	92	98	96	99	98
MIA	98	96	98	98	99	99
MKE	98	89	56	95	98	89
MSP	99	96	97	98	99	98
MSY	97	95	73	95	98	97
OKC	99	96	98	98	99	98
ORD	99	96	94	98	99	96
PBI	97	49	49	98	97	49
PHL	97	89	49	95	97	89
PHX	97	94	97	97	98	98
PIT	99	93	99	59	99	99
RDU	99	93	95	93	99	97
SDF	99	91	98	94	99	98
SJU	98	49	49	97	98	49
SLC	97	87	49	95	97	87
STL	98	94	98	97	99	98
TPA	98	99	99	99	99	99
TUL	99	94	98	96	99	98
Median	98	94	92	97	99	97

Table 7-15 gives the LLWAS + radar(s) results for the WSP airports. The LLWAS + WSP combination exceeds 90% detection probability at all but three airports. LLWAS + X-band combination does equally well.

TABLE 7-15
LLWAS + Radar(s) Microburst Detection Probability (%) at WSP Airports

Airport	WSP	NEXRAD	X-band	NEXRAD + WSP
ABQ	96	98	98	98
ALB	94	49	97	94
AUS	86	49	98	86
BDL	95	49	97	95
BHM	95	98	74	98
BUF	95	98	98	99
CHS	97	49	97	97
CID	96	49	98	96
DSM	94	98	97	98
ELP	97	51	98	97
FWA	94	53	97	94
GEG	93	97	97	98
GRR	95	99	98	99
GSO	96	49	86	96
HNL	98	49	96	98
HPN	95	49	96	95
HSV	97	49	96	97
ISP	89	97	97	97
JAX	92	99	98	99
LAX	92	49	96	92
LBB	96	98	98	99
MDT	91	49	92	91
MSN	93	49	96	93
ONT	95	49	97	95
ORF	91	49	94	91
PDX	95	49	90	95
RIC	91	71	94	92
ROC	96	49	98	96
SAT	96	95	98	96
SEA	93	49	97	93
SRQ	98	99	98	99
SYR	92	49	96	92
TOL	89	49	94	89
TUS	94	49	98	94
TYS	96	49	63	96
Median	95	49	97	96

Table 7-16 gives the LLWAS + radar results for the LLWAS airports.

TABLE 7-16
LLWAS + Radar Microburst Detection Probability (%) at LLWAS-RS Airports

Airport	NEXRAD	X-band
AGS	49	95
AVL	49	94
BIL	96	83
BTR	49	97
CAE	96	75
CHA	49	89
COS	89	91
CRW	98	82
CSG	49	94
DAB	49	97
FAY	49	96
FSD	94	96
FSM	99	97
GRB	97	95
GSP	99	97
JAN	98	94
LAN	49	96
LEX	49	98
LIT	98	96
LNK	79	97
MAF	98	97
MGM	49	96
MLI	97	92
MLU	49	97
MOB	98	97
OMA	95	97
PIA	61	96
PNS	49	97
PVD	95	98
ROA	49	90
RST	49	98
RSW	49	98
SAV	49	95
SFO	49	89
SGF	98	97
SHV	98	97
SPI	79	98
SUX	49	96
TLH	96	95
TRI	49	88
Median	70	96

Table 7-17 gives the LLWAS + radar(s) results for the other airports.

TABLE 7-17
LLWAS + Radar(s) Microburst Detection Probability (%) at Other Airports

Airport	TDWR	WSP	NEXRAD	X-band	NEXRAD + TDWR	NEXRAD + WSP
ABE	49	49	49	98	49	49
AMA	49	49	99	97	99	99
ASE	49	49	49	74	49	49
AVP	49	49	49	87	49	49
AZO	49	49	49	98	49	49
BGM	49	49	99	98	99	99
BIS	49	49	96	96	96	96
BOI	49	49	99	94	99	99
BTV	49	49	97	96	97	97
BUR	49	88	49	89	49	88
CAK	87	49	65	98	87	65
CMI	49	49	49	98	49	49
CRP	49	49	99	98	99	99
ERI	49	49	49	92	49	49
EVV	49	49	49	98	49	49
FAR	49	49	49	95	49	49
FNT	49	49	76	97	76	76
GCN	49	49	49	96	49	49
GFK	49	49	69	98	69	69
GPT	49	49	49	97	49	49
ILM	49	49	88	96	88	88
LFT	49	49	49	97	49	49
LGB	49	76	49	94	49	76
MBS	49	49	49	97	49	49
MHT	49	70	49	97	49	70
MYR	49	49	91	93	91	91
OAK	49	91	49	96	49	91
ORL	98	73	49	96	98	73
PDK	99	51	88	97	99	88
PHF	49	49	92	93	92	92
PIE	98	74	99	98	99	99
PWM	49	49	82	98	82	82
RNO	49	49	49	82	49	49
SAN	49	54	49	95	49	54
SBN	49	49	49	96	49	49
SFB	99	49	49	98	99	49
SJC	49	77	49	94	49	66
SMF	49	59	98	98	98	98
SNA	49	57	49	93	49	57
TWF	49	49	49	94	49	49
Median	49	49	49	96	49	69

Although the cost-benefit study of the wind-shear sensors uses the results of the upgraded TDWR, ASR-9, and NEXRAD, it is still informative to recompute the results for the non-upgraded radars. The pre- and post-upgrade figures can be used to predict the improvement in performance due to the upgrades, and the legacy numbers can also be compared to results collected previously in the field. The legacy results are listed in Tables 7-18 and 7-19 for the TDWR and WSP airports.

TABLE 7-18
Legacy Radar Wind-Shear Detection Probability (%) at TDWR Airports

Airport	Microburst			Gust Front		
	TDWR	WSP	NEXRAD	TDWR	WSP	NEXRAD
ADW	89	69	71	79	63	53
ATL	91	82	91	79	54	77
BNA	92	80	86	80	57	67
BOS	91	86	75	80	78	65
BWI	90	64	0	78	59	0
CLE	91	87	90	80	74	74
CLT	92	80	0	79	57	0
CMH	92	81	0	80	60	0
CVG	92	83	0	80	71	0
DAL	90	35	64	79	22	42
DAY	91	85	5	80	56	25
DCA	91	73	81	77	71	62
DEN	90	55	83	81	72	76
DFW	91	82	85	79	53	76
DTW	92	86	0	81	76	0
EWR	90	81	0	72	74	0
FLL	91	91	89	76	41	48
HOU	92	82	89	78	29	61
IAD	91	69	72	78	63	58
IAH	92	83	72	79	20	44
ICT	91	80	84	79	62	60
IND	90	91	91	80	72	75
JFK	91	84	0	80	78	0
LAS	78	57	0	49	46	0
LGA	91	27	0	80	37	0
MCI	92	94	13	81	81	27
MCO	92	92	0	78	63	15
MDW	92	23	88	81	35	80
MEM	92	64	89	79	49	72
MIA	90	82	90	76	31	53
MKE	91	68	13	80	50	35
MSP	92	89	89	81	76	78
MSY	91	82	57	78	34	41
OKC	92	87	89	79	70	69
ORD	91	74	69	80	55	79
PBI	89	0	0	78	0	0
PHL	88	66	0	75	39	4
PHX	89	78	89	49	45	72
PIT	91	84	91	81	77	79
RDU	92	73	84	79	50	66
SDF	92	65	90	79	46	71
SJU	91	0	0	74	0	0
SLC	88	59	0	56	43	0
STL	91	88	90	81	79	79
TPA	91	96	92	75	76	79
TUL	92	81	91	79	59	77
Median	91	81	74	79	57	56

TABLE 7-19
Legacy Radar Wind-Shear Detection Probability (%) at WSP Airports

Airport	Microburst		Gust Front	
	WSP	NEXRAD	WSP	NEXRAD
ABQ	90	91	61	63
ALB	83	0	74	0
AUS	70	0	42	15
BDL	86	0	77	0
BHM	79	90	58	79
BUF	86	91	75	75
CHS	84	0	24	0
CID	89	0	72	0
DSM	80	88	70	71
ELP	90	3	65	26
FWA	80	6	63	25
GEG	81	85	73	68
GRR	87	92	78	78
GSO	86	0	59	0
HNL	87	0	35	0
HPN	87	0	79	13
HSV	89	0	63	0
ISP	72	89	70	73
JAX	84	92	65	79
LAX	70	0	41	0
LBB	88	89	69	67
MDT	82	0	56	0
MSN	76	0	62	19
ONT	83	0	52	0
ORF	68	0	26	4
PDX	81	0	63	0
RIC	68	18	40	36
ROC	91	0	80	0
SAT	90	82	74	79
SEA	77	0	65	0
SRQ	96	91	78	80
SYR	77	0	67	0
TOL	66	0	46	0
TUS	81	0	48	0
TYS	88	0	68	0
Median	83	0	65	4

The median TDWR microburst detection probability is projected to improve by 6 percentage points after the upgrade, while the median gust-front detection probability is predicted to increase by 13 percentage points. Most of the improvement derives from the ability of the upgraded TDWR to reduce range-aliased obscuration of the interest region. Since the probability of range-aliased obscuration increases with distance from the radar (Appendix B) it makes sense that the gust-front case with its wider span of interest-region range benefits more than the microburst case. The legacy system performance, however, may be somewhat underestimated in this regard, because it does have a limited capacity for avoiding unwanted range-aliased signals in the ARENAs (Crocker 1988), whereas our model assumes that it does not.

As with any modeling effort, it is important to validate the results against empirical data. Table 7-20 shows the comparison of legacy TDWR microburst detection probabilities between field test (Klingle-Wilson et al. 1997; Evans and Weber 2000) and model results. The differences are no more than 3 percentage points in all cases, which is quite good given the small sample sizes used in the field tests. There is also a difference in the interest region, because the ARENAs were never 100% active at any given time during the field tests, whereas the model used the union of all possible ARENAs configurations. This is because a runway is, obviously, only used in one direction at a time, so the ARENAs for a runway at any time includes 3 miles arrival and 2 miles departure, not 3 miles on either side as does the union of all ARENAs. Thus, there may be a slight bias in the model toward detection probability underestimation due to this effect.

TABLE 7-20
Legacy TDWR Microburst Detection Probability (%) Comparison

Site	Empirical		Model
	P_d	P_{fa}	P_d
ATL	94	3	91
DCA	92	10	91
DEN	87	3	90
IAH	95	5	92
MCO	95	6	92
MEM	93	7	92

Gust-front detection performance results were also collected during the field experiments. However, the interest region was not defined to be an 18-km radius around the airport as we did in our model. Therefore, the results cannot be directly compared, as the shape and size of the interest region has a strong effect on the model results.

The WSP projects to show an improvement of about 7 percentage points for microburst and on the order of 10 percentage points for gust-front detection probabilities after the upgrade to the ASR-9. Unlike with the TDWR, there will be no enhanced capability for reducing range-aliased obscuration, so the increased performance is entirely due to the anticipated improvement in maximum clutter suppression capability from 48 dB to 60 dB (Table 3-1). However, in contrast to the TDWR upgrade, which is currently in a testing-for-approval phase, the ASR-9 upgrade has not yet begun and we do not know for sure whether the 60 dB target will be met.

There were field tests at four sites (ABQ, HSV, MCI, and MCO) to measure the wind-shear detection performance of the WSP using the prototype system (Weber et al. 1996). However, at ABQ, HSV, and MCI, the test radar was installed at locations significantly different from where the current ASR-9s are sited. Also, at HSV and MCI, the first-generation prototype was used, resulting in a sensitivity 5-15 dB lower than the operational system. Furthermore, an ASR-8 was used instead of an ASR-9 at HSV. The MCO field test began with the older WSP prototype on an ASR-8, but the system was upgraded and installed on an ASR-9 during the course of the experiment. The interest regions were not well defined for either microburst or gust front detection cases, making it difficult to do a meaningful direct comparison to the model results. For the record, the field test results at the two test sites with setups more consistent with the operational systems are P_d = 91%, P_{fa} = 6% at MCO, and P_d = 78% and P_{fa} = 18% at ABQ. The former is actually quite close to the model result (P_d = 92%). The latter is much worse than the model result (P_d = 90%) which is likely attributable to the operational radar being located in a depression to avoid the "severe ground clutter" (in the words of the field test report) observed by the prototype radar, as well as the interest area being limited to the ARENAs in the model.

There are other factors that can create a discrepancy between our model results and actual wind-shear detection performance. Microbursts and gust fronts are not the only types of wind shear that occur in the terminal environment and are hazardous to aviation. A line of thunderstorms can produce a linear divergence beneath the precipitation core, there can be an area of divergence behind a gust front, and gravity waves can generate significant wind shear (Crowe et al. 2003). The interaction of mesoscale and terrain-induced local flows can also result in a wide variety of wind shears. However, the microburst and gust front are the only two types of wind shear for which detection algorithms have been designed and deployed. Therefore, other kinds of wind shear may not be detected by the terminal wind-shear systems, but they may be reported as wind-shear encounters by pilots flying through them.

Radome attenuation during heavy rainfall is known to significantly degrade the radar sensitivity for the TDWR (and possibly the X-band radar), but this effect was not included in our model. The attenuation can also cause a wind-shear alert to not be issued because of the lack of VIL, even though the shear is detected in the wind field (Crowe et al. 2003).

Since we did not explicitly model the detection algorithms, we were not able to quantify site-dependent false alarm probabilities. High false alarm rates are, of course, just as undesirable as low detection probabilities. Phenomena that can trigger false alarms are bird flocks, bats flying out of caves, undealiased or falsely dealised velocities, unedited clutter residue, unfiltered range-aliased signals, etc. False alarm rates do not have a direct impact on the safety benefit estimates for wind-shear detection systems, but if they cannot be driven down to an acceptable level at a given site, they could induce the users to start ignoring alerts, which would certainly lower the system effectiveness. For delay reduction, false alarms can directly degrade the benefits by introducing unnecessary mitigation actions in terminal operations.

8. SUMMARY

As part of a comprehensive cost-benefit study, we developed an objective wind-shear detection probability estimation model for radar, lidar, and sensor combinations. This model allows a sensor- and site-specific performance analysis of deployed and future systems. The results showed that, as expected, the TDWR is the best single-sensor performer for microburst and gust-front detection among the considered wind-shear sensing systems. Also, preexisting TDWRs are close enough to four non-TDWR airports to provide satisfactory wind-shear detection capability (MCO for ORL and SFB, ATL for PDK, and TPA for PIE). On its own, the ASR-9 WSP cannot provide the required 90% microburst detection probability at many airports, even after the planned upgrade to its clutter suppression capability. The NEXRAD is too far away at a majority of airports to provide adequate wind-shear detection coverage. (On the flipside, this means that there are a significant number of airports where NEXRAD data can contribute to terminal wind-shear detection, especially for gust fronts, in which case the update rate does not need to be as fast as for microbursts.) And the typical LLWAS P_d for microbursts was low (~50%), because the anemometers usually only covered a fraction of the ARENAs. In fact, the only LLWAS airport with full microburst coverage was Denver (P_d = 97%).

Although the lidar by itself did not yield impressive wind-shear detection statistics, in combination with a radar it is projected to form an optimal configuration for wind-shear detection over the ARENAs and beyond. This is because the lidar excels at wind-shear detection under low reflectivity conditions when the radar signal is weak, and its collimated beam avoids ground clutter on which the radar's diverging antenna beam impinges. An LLWAS added to a radar can also improve the microburst detection probability over the ARENAs, but not to the same extent as a lidar if the radar detection probability is not very high. The LLWAS also cannot contribute to wide-area surveillance (beyond the ARENAs) because it is a collection of localized in situ instruments.

The estimated detection probability values computed in this study will feed into the overall cost-benefit calculation for the ground-based wind-shear detection systems. The conclusions are published in a separate Lincoln Laboratory project report (Hallowell et al. 2008).

APPENDIX A
SYNTHETIC CLUTTER MAP GENERATION

The synthetic clutter map generator was based on the angle-dependent model of Billingsley (2002), which assumes a Weibull distribution function for the unitless clutter coefficient σ°. The radar cross section relation between the clutter coefficient and volume reflectivity η is given by

$$\eta V = \sigma^\circ F^4 A_G \ , \tag{A-1}$$

where F is the propagation factor,

$$A_G = \frac{r\Delta\phi\Delta r}{\cos\theta_{dep}} \ , \tag{A-2}$$

is the ground area illuminated by the radar pulse, $\Delta\phi$ is the azimuth beamwidth, Δr is the pulse volume range extent, and the depression angle is

$$\theta_{dep} = \frac{\Delta h}{r} - \frac{r}{2R_{RE}} \ , \tag{A-3}$$

where Δh is the radar antenna altitude minus the ground clutter height at vector $\boldsymbol{r}$, and R_{RE} is the usual 4/3 earth radius to account for atmospheric refraction. Since the equivalent weather reflectivity is given by

$$Z_e = \frac{\eta\lambda^4}{\pi^5|K_w|^2} \ , \tag{A-4}$$

where λ is the radar wavelength and K_w is the complex refractive index of water, the equivalent clutter reflectivity can be written (in dBZ units) as

$$Z_C(\boldsymbol{r}) = 180 + 10\log\frac{\lambda^4 B^2(\theta_{off}(\boldsymbol{r}))\sigma^\circ(\boldsymbol{r})}{\pi^5\cos\theta_{dep}(\boldsymbol{r})|K_w|r\Delta\theta}, \tag{A-5}$$

where B is the one-way antenna beam power pattern (taken to be the only contributor to the propagation factor, since we do not have knowledge of the other factors), $\Delta\theta$ is the elevation beamwidth, and θ_{off} is the off-axis angle given by $\theta_{dep} + r/R_{RE}$. For the pencil-beam radars an idealized antenna pattern generated by a second-order Bessel function was used (Equation 3.2a, Doviak and Zrnić 1993) with a 30-dB sidelobe floor. For the ASR-9 a numerically defined pattern (Taylor and Brunins 1985) was used.

To generate $\sigma°(\boldsymbol{r})$ we utilized Matlab's WBLRND function, which produces random numbers following the Weibull distribution, given the two characteristic parameters, α, for scale, and β, for shape. The function call was made with

$$\alpha(\boldsymbol{r}) = \frac{10^{\sigma°_W(\boldsymbol{r})/10}}{\Gamma(1 + a_W(\boldsymbol{r}))} \ , \tag{A-6}$$

where Γ is the gamma function, and

$$\beta(\boldsymbol{r}) = \frac{1}{a_W(\boldsymbol{r})} \ . \tag{A-7}$$

Of course, $\sigma°_W(\boldsymbol{r}) = 0$ if the line of sight to location $\boldsymbol{r}$ (clutter visibility) is blocked. The quantities $\sigma°_W$ and a_W are tabulated in Billingsley (2002) according to surface type, relief type, depression angle (A-3), radar frequency, and spatial resolution (A-2), following extensive clutter data collection and analysis. In order to compute the depression angle, we needed the terrain elevation, which we obtained from Level 1 DTED. To make it as realistic as possible, we also added on top of this the predominant height of above-ground structures and vegetation taken from DFAD. (This augmented elevation data was also used to determine the clutter visibility.) An example of a clutter visibility and depression angle maps are shown in Figure A-1. The relief type was determined from the standard deviation of the terrain elevation within the resolution area. Finally, the 14 DFAD radar significance factors (RSFs) were assigned to one of Billingsley's five terrain types plus a new one (metal) as shown in Table A-1. See Table 4.2 in Billingsley (2002) for the corresponding values of $\sigma°_W$ and a_W. For metal, we assigned $\sigma°_W$ = -20 dB, and a_W = 1.8 and 1.3 at spatial resolutions of 1,000 and 1,000,000 m^2, for all radar frequencies of interest here. Additionally, if the areal feature record indicated tree coverage greater than 50%, then the RSF-based terrain type was overridden by the forest designation. An example of DFAD data and the corresponding extracted terrain type map is shown in Figure A-2.

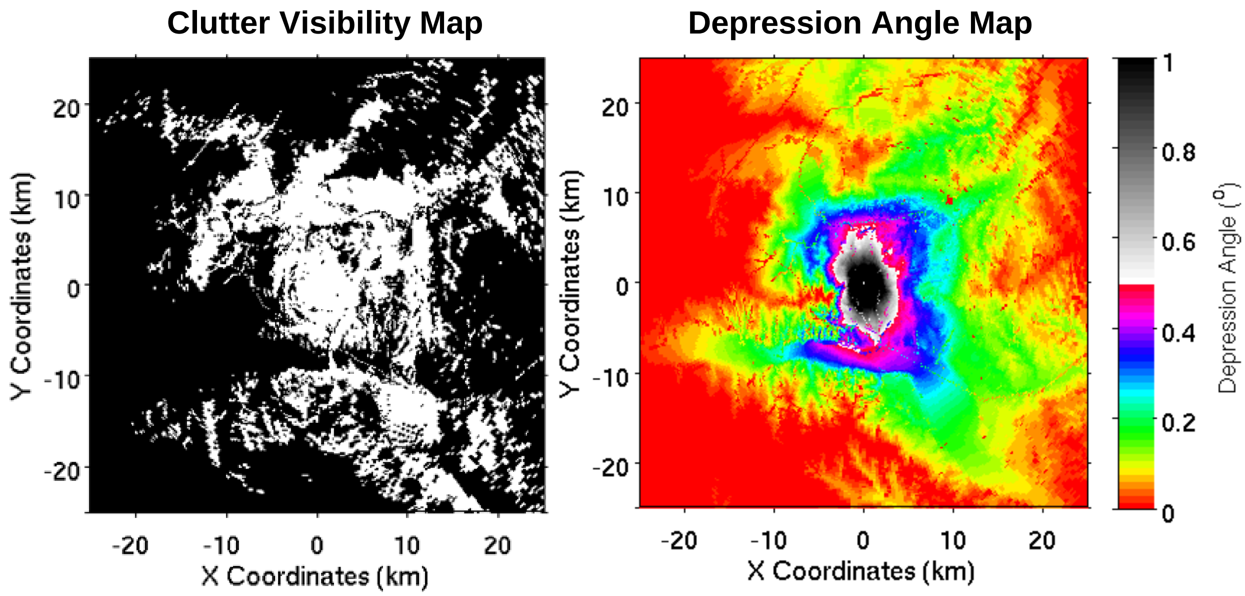

Figure A-1. Clutter visibility and depression angle maps computed for the TDWR at the PSF facility in Oklahoma City, OK.

TABLE A-1
Assignment of Terrain Type

Terrain Type	DFAD RSF
Desert, marsh, and grassland	Desert/sand, marsh, snow/ice, water
General rural	Earthen works, soil
Forest	Trees
Mountain	Rock
Urban	Part metal, stone/brick, composition, concrete, asphalt
Metal	Metal

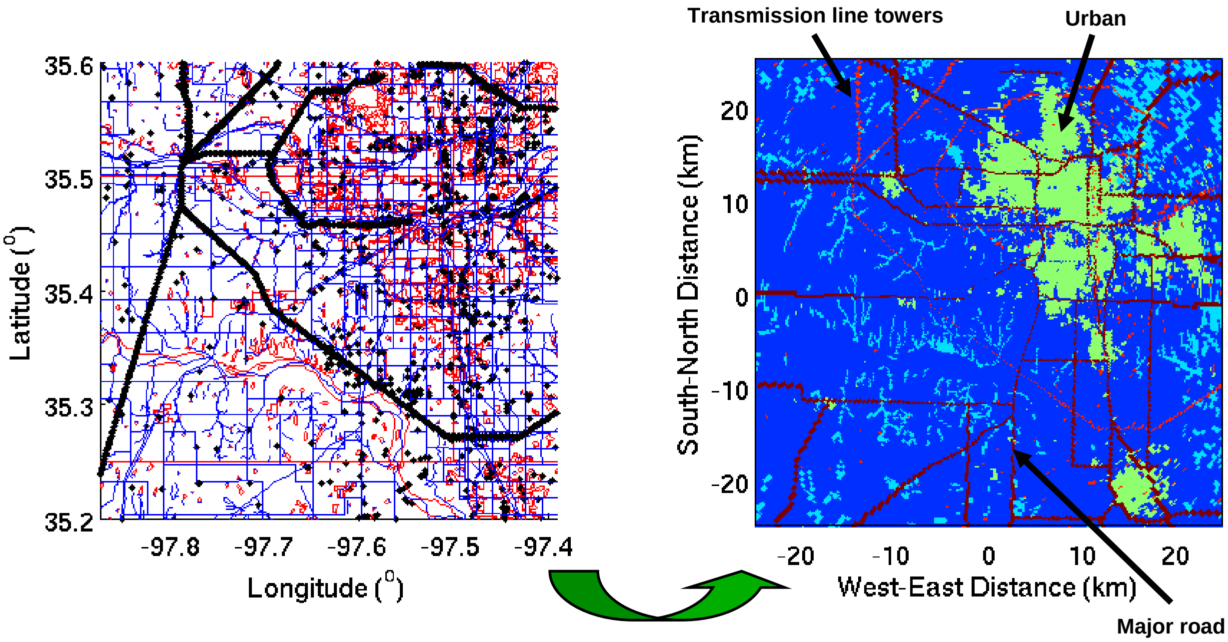

Figure A-2. DFAD data (left) and relevant features extracted and mapped to polar coordinates around the PSF TDWR (right).

Since persistent moving clutter is a key data quality issue, we kept track of the presence of roads by raising a flag in the presence of DFAD feature identification codes corresponding to elevated road, causeway, dual highway, or hard surface highway. We also computed the local orientation of the road segment, because Doppler filtering attuned to stationary clutter would fail to remove vehicular returns if their velocities had a significant component in the radar line-of-sight direction.

Another type of moving clutter, namely waves on open water (sea clutter), was not included in our model, and may have resulted in some underestimation of clutter residue at sites located near large bodies of water.

After the procedure outlined above was used to generate $Z_C(\boldsymbol{r})$, the clutter residue map was produced in the following manner. First, for non-road pixels, let the intermediate clutter filtered reflectivity be $Z_{CF}(\boldsymbol{r}) = Z_C(\boldsymbol{r}) - (S_{max} - L)$, where S_{max} is the maximum clutter suppression capability of the radar, L = 15 dB for the forest case, L = 10 dB for the urban and general rural case, L = 0 dB for the metal case, and L = 5 dB otherwise. The reduced clutter suppression capabilities are meant to reflect filter performance degradation due to spectral widening caused by clutter motion (e.g., wind-blown vegetation and signs, exhaust fans, etc.).

Second, for road pixels,

$$Z_{CF}(\boldsymbol{r}) = (Z_C(\boldsymbol{r}) - S_{\max})(1 - f_{\text{Road}}) + [Z_C(\boldsymbol{r}) - \min(0.2 Z_C(\boldsymbol{r}), S_{\max})] f_{\text{Road}} \,, \tag{A-8}$$

where

$$f_{\text{Road}} = \min\left[1, \max\left(0, \frac{\gamma - \gamma_0}{\gamma_1 - \gamma_0}\right)\right] , \tag{A-9}$$

γ is the angle between the radar line-of-sight and the normal to the road direction, γ_0 = 60°, and γ_1 = 75°. The rationale behind this expression is that traffic flows oriented perpendicular to the radar beam would present essentially zero Doppler shift, leading to maximum clutter suppression, whereas the Doppler shifts introduced as the road orientation comes into alignment with the radar beam would cause a loss of suppression. Buildings lining the road would also tend to block the traffic from view for road directions not aligned with the line of sight (the "building canyon" effect). The study of actual road clutter data indicated that the latter factor tends to dominate. The factor 0.2, γ_0, and γ_1 were chosen based on comparisons with real data.

One caveat with the road data is that the information density of the DFAD files varied with location. In other words, some places had more mapped roads in DFAD than others. The extreme case was Honolulu, where no road information was available in DFAD. Many of the western U.S. sites had sparse cartographic data. The southern Florida DFAD files, on the other hand, appeared to have more than an average density of mapped roads.

Third, we took the azimuthal beam-smearing effect into account. A mechanically scanned radar has an effective beamwidth, $\Delta\phi_{eff}$, that is dependent on the scan rate and dwell time in addition to the physical beamwidth (Figure 7.25, Doviak and Zrnić, 1993). The effective azimuthal beamwidths are given in Table A-2. The fraction of the two-way power within this effective beamwidth that is returned, not from the desired azimuthal sector, but from the one adjacent to it is approximately given by

$$p_{1s} = \left(\frac{2}{\Delta\phi_{eff}} \sqrt{\frac{\ln 2}{\pi}} \int_{-\infty}^{-\frac{\Delta\phi_{\sec}}{2}} e^{-\frac{4 \ln 2 y^2}{\Delta\phi_{eff}^2}} dy \right)^2 , \tag{A-10}$$

where $\Delta\phi_{sec}$ is the azimuthal sector width. This effect was incorporated into the final CREM reflectivity through the operation

$$Z_{CREM}(\boldsymbol{r}(\phi_i)) = 10 \log[p_{1s} 10^{Z_{CF}(\boldsymbol{r}(\phi_{i-1}))/10} + (1 - 2p_{1s}) 10^{Z_{CF}(\boldsymbol{r}(\phi_i))/10} + p_{1s} 10^{Z_{CF}(\boldsymbol{r}(\phi_{i+1}))/10}], \tag{A-11}$$

where ϕ_i is the i^{th} azimuth beam position.

TABLE A-2

Effective Azimuthal Beamwidth

Radar System	Beamwidth
TDWR	1.2°
ASR-9 WSP	2.5°
NEXRAD	1.4°
LMCT X-band	2°

Figure A-3 shows a comparison between the actual reflectivity field on a clear day recorded by the PSF TDWR at 0.3° elevation and the corresponding synthetic CREM. The clutter suppression capability of the TDWR is so good in this case that most of the residue is due to moving clutter on roads. The synthetic CREM manages to capture many of the essential details correctly. Because idealized antenna patterns are used and because the DFAD does not contain every feature that presents a cross section to the radar, there is a tendency for the synthetic CREM to have lower reflectivity in some places compared to the real map. Also, since the actual reflectivity data comes from one scan, some of the residue may be transient. Overall, the comparison is fairly good.

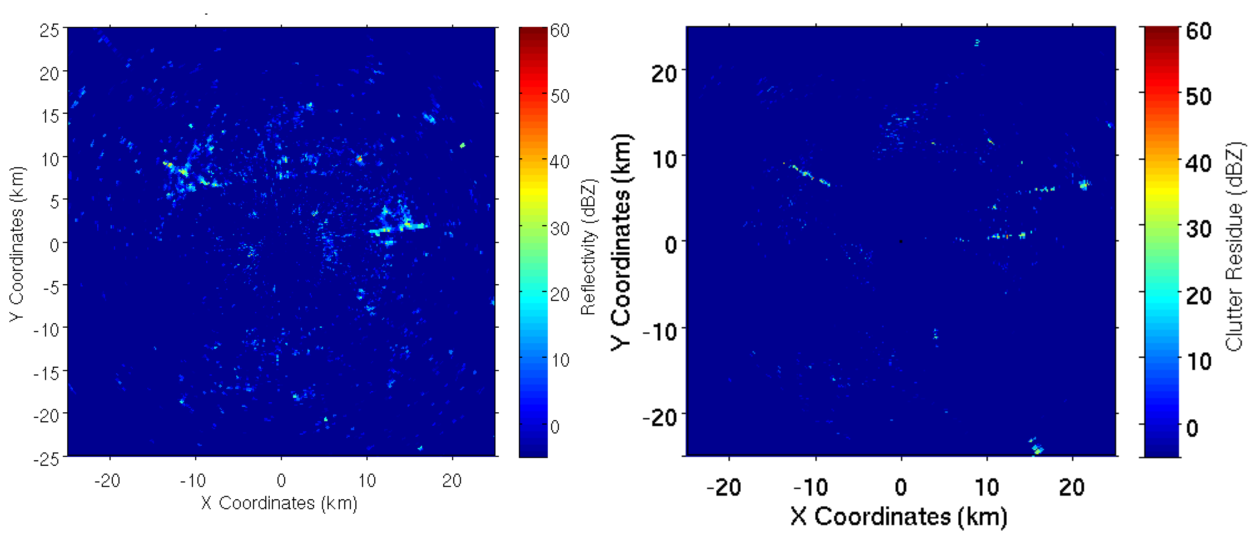

Figure A-3. Clear-day reflectivity (left) and synthesized CREM (right) for the PSF TDWR at 0.3° elevation.

APPENDIX B
SIMULATION OF RANGE-ALIASING STATISTICS

In order to compute the statistics of range-aliased weather signals, one needs to know the spatial variability of weather reflectivity. One can either use actual archived data or simulated data for this purpose. The advantage of the former is that the data are real; the disadvantage is that the characteristics of the radar that was used to collect the data are convolved in the results. In other words, the "actual" reflectivity data do not necessary correspond to truth given uncorrected radar-dependent effects such as beam-filling loss and precipitation attenuation. With simulated data, one can start out with the same reference reflectivity field then add in the radar-dependent effects. This is the approach we chose.

To generate a one-dimensional (1D) reflectivity field, we appropriated a multifractal model proposed by Tessier et al. (1993). Many natural phenomena, including atmospheric processes, manifest scaling and intermittency features that are not well characterized by Gaussian statistics. The multifractal cascade model is an alternative that has had success characterizing such processes. In this model, three parameters are used to define the statistical properties of the desired (nonconservative) field: H, a measure of the deviation of the resulting field from the conserved field, c_1, the codimension of the mean process that characterizes the sparseness of the conserved field, and α_L, the Levy index (degree of multifractality). We describe the steps briefly here. Further details and explanation can be found in Wilson et al. (1991).

First, a vector is generated with length n corresponding to the number of range gates desired. The vector elements are extremal Levy random variables given by

$$y_j = \frac{\xi}{m^{1/\alpha_L}} \sum_{i=1}^{m} \left(\frac{\alpha_L}{\alpha_L - 1} - w_{ij}^{-1/\alpha_L} \right) , \tag{B-1}$$

where m is an integer sufficiently large (say, 30) for convergence, w_{ij} are elements of an m x n matrix of uniformly distributed random numbers between 0 and 1, and

$$\xi = \left[\frac{C_1}{\Gamma(2-\alpha_L)} \right]^{1/\alpha_L} . \tag{B-2}$$

Next, this subgenerator is fractionally integrated (power-law filtered in the Fourier spectral domain):

$$G_s = Y_s \left| k_s \right|^{\frac{1}{\alpha_L} - 1} , \tag{B-3}$$

where k is the wavenumber. Capitalizations denote the discrete Fourier transform (DFT) of their lower case counterparts, with subscript s the spectral index. Then the inverse DFT is taken and the result exponentiated,

$$q_j = \pi^{\frac{c_1}{1-\alpha_L}} e^{g_j} \quad , \tag{B-4}$$

to yield a conservative field that is dependent on both c_1 and α_L. Finally, another fractional integration using H is performed,

$$\Phi_s = Q_s |k_s|^{-H/2} \quad , \tag{B-5}$$

and the inverse DFT is taken to arrive at ϕ_j. To normalize the values to match a typical reflectivity PDF, we multiplied ϕ_j by 15. Radar reflectivity data during a convective storm were analyzed by Tessier et al. (1993) to obtain values of $H = 0.32$, $c_1 = 0.12$, and $\alpha_L = 1.4$. We used these values in our simulation runs.

Starting with a 1D array of synthesized reflectivity values using the technique described above, we included effects that would diminish the reflectivity observed by a radar. (We used a 460-element array with 1-km range-gate spacing for simplicity.) First, due to Earth's curvature and finite height extent of weather, a decreasing fraction of the radar beam would be filled by weather returns with increasing range. This is the beam-filling loss effect, and the way to quantify it is discussed in Appendix B of Cho and Martin (2007). To be conservative (i.e., to err on the side of more range-aliased interference) we took the weather vertical extent to be 12 km (many storms top out well below this height). Second, we accounted for atmospheric attenuation (including precipitation) effects, since this can be an important contributor to reflectivity loss, especially at X band. The two-way attenuation coefficients (dB/km) that we used were: $0.016 + 1.3 \times 10^{-5} Z^{0.69}$ for S band, $0.019 + 5.0 \times 10^{-5} Z^{0.75}$ for C band, and $0.028 + 1.5 \times 10^{-4} Z^{0.86}$ for X band, where Z is the reflectivity in linear units. C- and S-band attenuation effects were included here due to the long distances (up to 460 km) involved.

We then converted the reflectivity values to SNRs. Each first-trip gate SNR was compared to all corresponding out-of-trip gate SNRs. For the ASR-9, which does not have range-fold protection, the gate was marked as obscured if the first-trip "interest area" SNR was less than 10 times the overlaid signal. For the other radars, which (will) have phase-code and/or multi-PRI processing for range ambiguity resolution, the worst-case scenario was assumed, i.e., that clutter filtering was necessary. In this case, the gate was marked as obscured if the first-trip "interest area" SNR was less than the overlaid signal. If clutter filtering was ultimately not necessary, it was assumed that the range-ambiguity resolution algorithm will work well (see 3-3). We write "interest area" in quotes, because we did not perform this simulation per radar for each site due to the unreasonable amount of time involved. Instead we used the range gates that fell within the average distances to the interest area edges. The first-trip ranges we assumed were 115 km (ASR-9 and NEXRAD), 90 km (TDWR), and 60 km (X band). The fraction of obscured gates within the "interest area" was computed, and this Monte Carlo simulation was repeated many times (we did it 1000 times) to generate the probability of range-fold obscuration, F_{RF}.

An example of a simulation run for the TDWR is shown in Figure B-1. In this realization, the first-trip signal dominates for the first half of the unambiguous range, while the second-trip signal is the strongest one in the second half of the unambiguous range. There is even a short stretch in the middle where the fifth-trip signal is strongest. This is not a fluke, as fifth-trip signal from a far away storm has been known to contaminate first-trip echoes in real TDWR data.

The resulting probabilities that range-aliased signals will interfere with first-trip signals in the interest area are listed in Table B-1. The factors favoring range aliasing are high PRF (short unambiguous range) and narrow antenna beam (less beam-filling loss with range). The factors working against range aliasing are closeness to the interest region (r^{-2} signal fall-off favors close range) and precipitation attenuation (far away storms harder to see). The results with the most uncertainty are those of the NEXRAD, because its distance to the airport varies widely, whereas our calculation assumed an average distance. If it is closer than the average distance F_{RF} will be less, and if it is farther than the average distance F_{RF} will be more. Note, however, that the values in Table B-1 are not the end of the story, as the *effective* range-fold obscuration probability after ambiguity mitigation procedures have been applied depends on the presence of ground clutter (the F_{SCR} term in (3-2)) for both phase-code and multi-PRI range-ambiguity mitigation techniques (Cho et al. 2005). Since ground clutter tends to be more severe at short range, closeness to the interest region favors range-fold obscuration with the mechanism. Ground clutter is, of course, site dependent, so this factor was calculated for each radar at each site.

TABLE B-1

Range Aliasing Probabilities

Radar	Interest Area	
	ARENAs	18-km Radius Around Airport
TDWR	2%	8%
ASR-9	0.5%	3%
NEXRAD	3%	9%
LMCT X-band	0.3%	3%

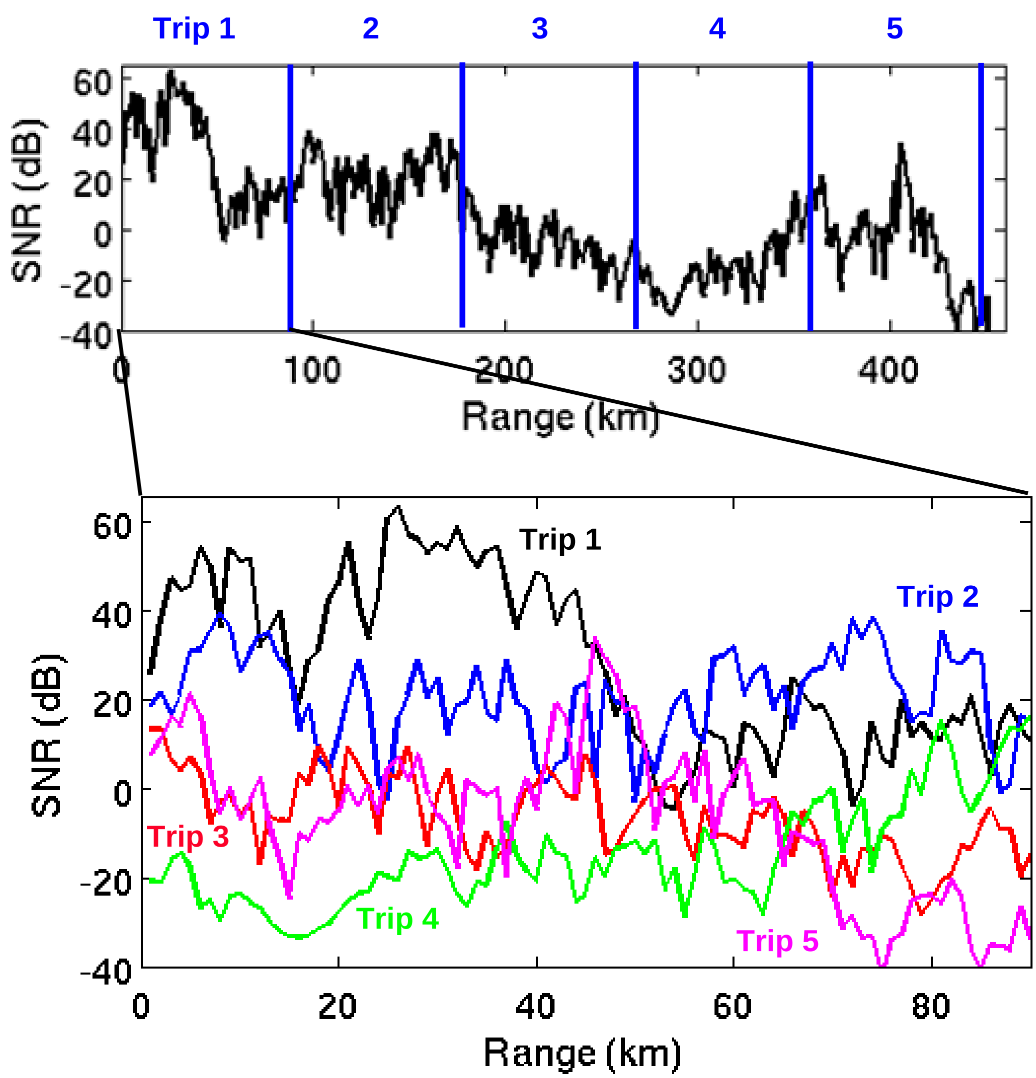

Figure B-1. Simulated precipitation SNR vs. range for a TDWR using a PRF of 326 Hz (top) and 1670 Hz (bottom). The signal contribution from each trip (range aliased for trip > 1) is shown separately in the lower figure.

APPENDIX C
ATTENUATION DUE TO PRECIPITATION

The minimum detectable reflectivity vs. range can be written in the form

$$Z_{\min}(r) = Cr^2 10^{\kappa r/10} \ , \qquad \text{(C-1)}$$

where C is a constant containing all the radar-specific parameters and κ (dB/km) is the two-way atmospheric attenuation coefficient. There is no further complication if κ is assumed to be constant, which is fine under clear-air conditions. However, κ can significantly rise over the nominal clear-air value in the presence of precipitation, especially at shorter wavelengths like X band. It is possible to relate κ to the rain rate, R (mm/h),

$$\kappa(R) = \kappa_a + a_1 R^{b_1} \ , \qquad \text{(C-2)}$$

where κ_a is the clear-air attenuation coefficient, and a_1 and b_1 are empirically fitted constants that vary with radar frequency. We use $\kappa_a = 0.028$, $a_1 = 0.2$ and $b_1 = 1.21$ for X band (Doviak and Zrnić, 1993). The rain rate, in turn, can be expressed via the Z-R relation,

$$Z(R) = a_2 R^{b_2} \ . \qquad \text{(C-3)}$$

We used $a_2 = 300$ and $b_2 = 1.4$. Putting (C-2) and (C-3) together, we get

$$\kappa(Z) = \kappa_a + a_1 \left(\frac{Z}{a_2} \right)^{b_1/b_2} \ . \qquad \text{(C-4)}$$

If we assume that the reflectivity is constant between the radar and the range of interest (which may be fine if the range is not very far) then (C-4) inserted into (C-1) yields a nonlinear equation with two possible solutions that represent the minimum ($Z_{\min}$) and maximum ($Z_{\max}$) detectable reflectivity. These were the values that went into forming Z_{lo} and Z_{hi} of (3-1) for the X-band radar.

GLOSSARY

ACF	Airport Configuration File
ARENAs	Areas Noted for Attention
ASR-9	Airport Surveillance Radar-9
CREM	Clutter Residue Map
DFAD	Digital Feature Analysis Data
FAA	Federal Aviation Administration
HNL	Honolulu
LAS	Las Vegas
LLWAS-RS	Low Altitude Wind Shear Alert System Relocation/Sustainment
LMCT	Lockheed Martin Coherent Technologies
MCO	Orlando
MIGFA	Machine Intelligent Gust Front Algorithm
MPAR	Multi-mission Phased Array Radar
NAS	National Airspace System
NCAR	National Center for Atmospheric Research
NEXRADs	Next Generation Weather Radar
PDF	Probability Distribution Function
PHX	Phoenix
PIT	Pittsburgh
SLC	Salt Lake City
SLEPs	Service Life Extension Programs
TDWR	Terminal Doppler Weather Radar
WSP	Weather Systems Processor
WSR-88D	Weather Surveillance Radar-1988 Doppler

REFERENCES

Billingsley, J. B, 2002: *Low-Angle Radar Land Clutter: Measurements and Empirical Models*. William Andrews, 722 pp.

Biron, P. J., and M. A. Isaminger, 1991: High resolution microburst outflow vertical profile data from Huntsville, Alabama, and Denver, Colorado. Project Rep. ATC-163, MIT Lincoln Laboratory, Lexington, MA, 214 pp.

Chan, P. W., C. M. Shun, and K. C. Wu, 2006: Operational LIDAR-based system for automatic windshear alerting at the Hong Kong International Airport. Preprint, *12th Conf. on Aviation, Range, and Aerospace Meteorology*, Atlanta, GA, Amer. Meteor. Soc., http://ams.confex.com/ams/pdfpapers/100601.pdf.

Cho, J. Y. N., and B. D. Martin, 2007: Technical assessment of the impact of decommissioning the TDWR on terminal weather services. Project Rep. ATC-331, MIT Lincoln Laboratory, Lexington, MA, 68 pp.

Cho, J. Y. N., G. R. Elkin, and N. G. Parker, 2005: Enhanced radar data acquisition system and signal processing algorithms for the Terminal Doppler Weather Radar. Preprints, *32nd Conf. on Radar Meteorology*, Albuquerque, NM, Amer. Meteor. Soc., P4R.8, http://ams.confex.com/ams/pdfpapers/96018.pdf.

Cole, R. E., 1992: Terminal Doppler Weather Radar/Low-Level Wind Shear Alert System integration algorithm specification version 1.1. Project Rep. ATC-187, MIT Lincoln Laboratory, Lexington, MA, 36 pp.

Cole, R. E., and R. F. Todd, 1996: A comparative performance study of TDWR/LLWAS 3 integration algorithms for wind shear detection. Preprints, *Workshop on Wind Shear and Wind Shear Alert Systems*, Amer. Meteor. Soc., Oklahoma City, OK, 43-52.

Crocker, S. C., 1988: TDWR PRF selection criteria. Project Rep. ATC-147, MIT Lincoln Laboratory, Lexington, MA, 57 pp.

Crowe, B., D. Miller, J. Shaw, and B. Collins, 2003: An examination of wind shear alert integration at the Dallas/Ft. Worth International Airport (DFW). Project Rep. ATC-309, MIT Lincoln Laboratory, Lexington, MA, 56 pp.

Delanoy, R. L., and S. W. Troxel, 1993: Machine intelligent gust front algorithm. Project Rep. ATC-196, MIT Lincoln Laboratory, Lexington, MA, 129 pp.

Doviak, R. J., and D. S. Zrnić, 1993: *Doppler Radar and Weather Observations*. 2nd Ed., Academic Press, 562 pp.

Evans, J. E., and M. E. Weber, 2000: Weather radar development and application programs. *Linc. Lab. J.*, **12**, 367-382.

Hallowell, R. G., J. Y. N. Cho, S. Huang, and M. E. Weber, 2008: Wind shear system cost benefit analysis update. Project Rep. ATC-3XX, MIT Lincoln Laboratory, Lexington, MA, xx pp.

Hannon, S. M., 2004: Pulsed Doppler lidar for terminal area monitoring of wind and wake hazards. Preprints, *11th Conf. on Aviation, Range, and Aerospace Meteorology*, Amer. Meteor. Soc., Hyannis, MA, P4.21, http://ams.confex.com/ams/pdfpapers/87757.pdf.

Heiss, W. H., D. L. McGrew, and D. Sirmans, 1990: NEXRAD: Next Generation Weather Radar (WSR-88D). *Microwave J.*, **33**, 79-98.

Klingle-Wilson, D., and M. F. Donovan, 1991: Characteristics of gust fronts. Preprints, 4th Int. Conf. on Aviation Weather Systems, Paris, France, Amer. Meteor. Soc., 387-392.

Klingle-Wilson, D., M. Isaminger, and C. Keohan, 1997: Report on product performance for the Terminal Doppler Weather Radars (TDWRs) at Washington National Airport and Memphis and Orlando International Airports. Project Rep. ATC-246, MIT Lincoln Laboratory, Lexington, MA, 42 pp.

Martin Marietta, 1994: Wind shear systems cost-benefit and deployment study: System engineering and integration contract for implementation of the National Airspace System plan. ATC-92-1201, Martin Marietta Air Traffic Systems, 91 pp.

Michelson, M., W. W. Shrader, and J. G. Wieler, 1990: Terminal Doppler Weather Radar. *Microwave J.*, **33**, 139-148.

Patel, N. K., and R. W. Macemon, 2004: NEXRAD Open Radar Data Acquisition (ORDA) signal processing and signal path. Preprints, *20th Int. Conf. on Interactive Information and Processing Systems for Meteorology, Oceanography, and Hydrology*, Seattle, WA, Amer. Meteor. Soc., 5.4, http://ams.confex.com/ams/pdfpapers/70926.pdf.

Sachidananda, M., and D. S. Zrnić, 1999: Systematic phase codes for resolving range overlaid signals in a Doppler weather radar. *J. Atmos. Oceanic Technol.*, **16**, 1351-1363.

Smalley, D. J., B. J. Bennett, and R. Frankel, 2005: MIGFA: The machine intelligent gust front algorithm for NEXRAD. Preprints, *32nd Conf. on Radar Meteorology*, Albuquerque, NM, Amer. Meteor. Soc., http://ams.confex.com/ams/pdfpapers/96098.pdf.

Taylor, J. W., Jr., and G. Brunins, 1985: Design of a new airport surveillance radar (ASR-9). *Proc. IEEE*, **72**, 284-289.

Tessier, Y., S. Lovejoy, and D. Schertzer, 1993: Universal multifractals: Theory and observations for rain and clouds. *J. Appl. Meteorol.*, **32**, 223-250.

Weber, M. E., and M. L. Stone, 1995: Low altitude wind shear detection using airport surveillance radars. *IEEE Aerosp. Electron. Syst. Mag.*, **10**, 3-9.

Weber, M. E., and S. W. Troxel, 1994: Assessment of the weather detection capability of an airport surveillance radar with solid-state transmitter. Project Rep. ATC-209, MIT Lincoln Laboratory, Lexington, MA, 71 pp.

Weber, M. E., J. A. Cullen, S. W. Troxel, and C. A. Meuse, 1996: ASR-9 weather system processor (WSP): Wind shear algorithms performance assessment. Project Rep. ATC-247, MIT Lincoln Laboratory, Lexington, MA, 42 pp.

Weber, M. E., M. A. Isaminger, C. Meuse, S. V. Vasiloff, and T. Shepherd, 1995: Comparative analysis of ground-based wind shear detection radars. *Proc. 1995 Int. Radar Conf.*, IEEE, Alexandria, VA, 486-495.

Weber, M. E., J. Y. N. Cho, J. S. Herd, J. M. Flavin, W. E. Benner, and G. S. Torok, 2007: The next-generation multimission U.S. surveillance radar network. *Bull. Amer. Meteor. Soc.*, **88**, 1739-1751.

Wilson, F. W., and R. E. Cole, 1993: LLWAS II and LLWAS III performance evaluation. Preprints, *5th Conf. on Aviation Weather Systems*, Amer. Meteor. Soc., Vienna, VA, 204-208.

Wilson, F. W., and R. H. Gramzow, 1991: The redesigned Low Level Wind Shear Alert System. Preprints, *4th Int. Conf. on Aviation Weather Systems*, Paris, France, 370.

Wilson, J., D. Schertzer, and S. Lovejoy, 1991: Continuous multiplicative cascade models of rain and clouds. In *Non-Linear Variability in Geophysics*, D. Schertzer and S. Lovejoy, Eds., Kluwer Academic, pp. 185-207.

Wolfson, M., D. Klingle-Wilson, M. Donovan, J. Cullen, D. Neilley, M. Liepins, R. Hallowell, J. DiStefano, D. Clark, M. Isaminger, P. Biron, and B. Forman, 1990: Characteristics of thunderstorm-generated low altitude wind shear: A survey based on nationwide Terminal Doppler Weather Radar testbed measurements. *Proc. 29th Conf. on Decision and Control*, IEEE, Honolulu, HI, 682-688.